Combining instrument inversions for sub-10 nm aerosol number size-distribution measurements

Stolzenburg, Dominik

2022-01

Stolzenburg , D , Ozon , M , Kulmala , M , Lehtinen , K E J , Lehtipalo , K & Kangasluoma , J 2022 , ' Combining instrument inversions for sub-10 nm aerosol number size-distribution measurements ' , Journal of Aerosol Science , vol. 159 , 105862 . https://doi.org/10.1016/j.jaerosci.2021.105862

http://hdl.handle.net/10138/341741
https://doi.org/10.1016/j.jaerosci.2021.105862

Journal of Aerosol Science 159 (2022) 105862

Contents lists available at ScienceDirect

Journal of Aerosol Science

journal homepage: www.elsevier.com/locate/jaerosci

Combining instrument inversions for sub-10 nm aerosol number size-distribution measurements

Dominik Stolzenburg [a,*], Matthew Ozon [b], Markku Kulmala [a], Kari E.J. Lehtinen [b,c], Katrianne Lehtipalo [a,d], Juha Kangasluoma [a,**]

[a] Institute for Atmospheric and Earth System Research/Physics, University of Helsinki, 00014, Helsinki, Finland
[b] Department of Applied Physics, University of Eastern Finland, 70211, Kuopio, Finland
[c] Finnish Meteorological Institute, Kuopio, Finland
[d] Finnish Meteorological Institute, Helsinki, Finland

ARTICLE INFO

Keywords:
particle size-distribution
size-distribution inversion
Inverse problems
Combining instruments
New particle formation
Sub-10 nm

ABSTRACT

Resolving aerosol dynamical processes in the sub-10 nm range is crucial for our understanding of the contribution of new particle formation to the global cloud condensation nuclei budget or air pollution. Accurate measurements of the particle size distribution in this size-range are challenging due to high diffusional losses and low charging and/or detection efficiencies. Several instruments have been developed in recent years in order to access the sub-10 nm particle size distribution; however, no single instrument can provide high counting statistics, low systematic uncertainties and high size-resolution at the same time. Here we compare several data inversion approaches that allow combining data from different sizing instruments during the inversion and provide python/Julia packages for free usage of the methods. We find that Tikhonov regularization using the L-curve method for optimal regularization parameter estimation gives very reliable results over a wide range of tested data sets and clearly improves standard inversion approaches. Kalman Filtering or regularization using a Poisson likelihood can be powerful tools, especially for well-defined chamber experiments or data from mobility spectrometers only, respectively. Nullspace optimization and non-linear iterative regression are clearly inferior compared to the aforementioned methods. We show that with regularization we can reconstruct the size-distribution measured by up to 4 different mobility particle size spectrometer systems and several particle counters for datasets from Hyytiälä and Helsinki, Finland, revealing the sub-10 nm aerosol dynamics in more detail compared to a single instrument assessment.

1. Introduction

The smallest aerosol particles below 10 nm are of crucial interest in climate science (Carslaw et al., 2013), nanotechnology (Swihart, 2003) and they also can be related to air pollution (Guo et al., 2014; Kulmala et al., 2021) and possibly influence human health (Pedata et al., 2015). Also in this size range – particularly in sub-3 nm – chemistry and physics of aerosol particles are tightly interlinked. Aerosol measurements of this cluster-particle transition regime remain a challenge as classical optical detection is

* Corresponding author.
** Corresponding author.
E-mail addresses: dominik.stolzenburg@helsinki.fi (D. Stolzenburg), juha.kangasluoma@helsinki.fi (J. Kangasluoma).

https://doi.org/10.1016/j.jaerosci.2021.105862
Received 30 May 2021; Received in revised form 17 August 2021; Accepted 19 August 2021
Available online 28 August 2021

unfeasible at typical ambient concentrations (Bauer, Amenitsch, Baumgartner, Köberl, & Rentenberger, 2019; Vazquez-Pufleau & Winkler, 2020). Aerosol size-distributions are often inferred using differential mobility analysers (DMAs), which require charged aerosol particles (Flagan, 1998). However, low charging probabilities (Wiedensohler, 1988), high diffusional losses during sampling and low detection efficiencies cause very low counting statistics in atmospheric measurements in the sub-10 nm range. Moreover, detection of particles in this size range with condensation particle counters depends on the chemical composition of the sampled aerosol (Kangasluoma et al., 2013; Wlasits et al., 2020), which is usually unknown.

Several recent developments have improved the instrumentation for sub-10 nm aerosol size distribution measurements. The particle size magnifier (PSM) in scanning mode (Vanhanen et al., 2011) does not rely on particle charging, which improves the signal-to-noise ratio, but as the sizing is based on particle activation, it is very sensitive to aerosol chemical composition and only achieves a limited time-resolution. The neutral clusters and air ion spectrometer (NAIS; Manninen et al., 2009) also achieves a good signal-to-noise ratio due to the application of unipolar charging and integration of the detecting electrometers into the DMA but cannot reliably measure below 2.5 nm due to large charger ions disturbing the signal. Also new versions of classical mobility particle size spectrometers have been developed to face the challenges of sub-10 nm measurements (e.g. Jiang et al., 2011a; Kangasluoma et al., 2018). The DMA-train (D. Stolzenburg, Steiner, & Winkler, 2017) even uses six DMAs in parallel to gain higher counting statistics at the six fixed measured sizes. However, no instrument alone is able to cover the dynamics of atmospheric relevant processes over the full size-range with high sensitivity, size- and time-resolution. This still limits e.g. our understanding of the growth and nucleation mechanisms during new particle formation (Kulmala et al., 2013). Different instruments offer different advantages and disadvantages and the agreement between instruments in the sub-10 nm range remains a big challenge (Kangasluoma et al., 2020).

While the instrumental development has been progressing over the last few years, the commonly applied data analysis and inversion techniques in the sub-10 nm range have mostly remained relatively simple. However, it is known that the simplifications made within the often applied point-by-point inversion (M. R. Stolzenburg & McMurry, 2008) can lead to significant systematic errors (Kangasluoma & Kontkanen, 2017). Moreover, it does neither allow for the combination of several instruments in the same inversion procedure nor accounts for a certain correlation of neighbouring size channels due to typically rather smooth atmospheric aerosol size-distributions. Kandlikar and Ramachandran (1999) gave a detailed overview of more sophisticated inversion techniques. Recently, Sipkens et al. (2020) have presented inversion algorithms for 2-dimensional mass-mobility measurements, including iterative approaches (Markowski, 1987; Twomey, 1975) and regularization methods (Tikhonov & Arsenin, 1977; Wolfenbarger & Seinfeld, 1990). However, neither of the presented methods is widely applied in the sub-10 nm size range nor is any of them used to combine several instruments for particle sizing. Moreover, none of the methods takes into account that subsequent size-distribution measurements are also correlated, as measurement cycles are in many situations faster than the changes of the ambient aerosol (besides fast changing urban settings, e.g. Mølgaard, Vanhatalo, Aalto, Prisle, and Hämeri (2016)). Recently, Ozon, Seppänen, Kaipio, and Lehtinen (2021) have developed a fixed interval Kalman smoother (FIKS) for recovering process rates of aerosol chamber experiments. Kalman filtering has also been applied to aerosol size-distribution inversion (Viskari, Asmi, Kolmonen, et al., 2012; Voutilainen & Kaipio, 2001) and even for a combination of different instruments (Viskari, Asmi, Virkkula, et al., 2012), but again application for the critical sub-10 nm range is lacking. Finally, all above methods are based on Gaussian approximations of the uncertainties, which is not valid for the low count rates often measured in the sub-10 nm range. Here, we compare six inversion approaches with respect to their ability to combine several instruments, including some well-established approaches (Fiebig, Stein, Schröder, Feldpausch, & Petzold, 2005; Lloyd, Taylor, Lawson, & Shields, 1997; Markowski, 1987), a recently developed method (Ozon, Seppänen, et al., 2021) and additionally we develop a Poisson formulation of the regularization approach. We test these inversion procedures with simulated particle size distributions and show their applicability to ambient observations, demonstrating that combining instruments into one inversion procedure can enhance our understanding of the sub-10 nm aerosol dynamics.

2. Inversion methods

The inversion of n aerosol measurement outcomes to an aerosol particle size distribution (PSD; $f(d_p)$) can be described by the inversion of so-called Fredholm integrals of the first kind:

$$y_i = \int K_i(d_p) \cdot f(d_p)\, \mathrm{d}d_p + \varepsilon_i. \tag{1}$$

where K_i are the kernel (or response, or transfer) functions, describing the response y_i of the instrument channel i to a monodisperse aerosol sample of size d_p. ε_i is the error in channel i causing deviations from an ideal solution, which can include both a measurement error and an error in the estimate of K_i. Eq. (1) can be rewritten compactly in matrix notation by describing the measurement outcomes in vector notation and discretizing the kernel and size-distribution:

$$\vec{y} = K\vec{f} + \vec{\varepsilon}. \tag{2}$$

The vector $\vec{\varepsilon}$ can now additionally account for an error introduced by the discretization compared to the exact integral of Eq. (1). The discretization of the Kernel and size-distribution can be done in different ways, either into a set of base functions with m parameters which can describe the shape of the size distribution and could reduce the number of unknowns to the number of measurements ($m \leq n$, e.g. Hagen & Alofs, 1983) or into m sizes using numerical quadrature, usually logarithmically spaced with $m > n$. The problem described by Eq. (2) is ill-posed and usually also underdetermined (for $m > n$). Therefore, it cannot be solved by direct matrix inversion but additional constraints are needed. Certainly, Eq. (2) requires a non-negativity solution for the aerosol

size-distribution, i.e. $\vec{f} \geq 0$.

The problem can also be formulated through statistical arguments, i.e. a Bayesian approach (Ramachandran and Kandlikar, 1996). We start from the probability of measuring the signal $\vec{y}$ given the instrument kernel functions K and size-distribution $\vec{f}$, $P(\vec{y}|K,\vec{f}) = \prod_{i=0}^{n} P(y_i|K_i,\vec{f})$. The idea is to find the size-distribution $\vec{f}$ which maximizes the probability of obtaining the measurement $\vec{y}$ given K and $\vec{f}$, i.e. maximizing $P(\vec{y}|K,\vec{f})$. As in ill-posed problems this can lead to oscillatory solutions, it is useful to incorporate additional prior knowledge, e.g. on the shape of $\vec{f}$ into the problem. This can be implemented by formulating an a priori probability of $\vec{f}$, i.e. $P(\vec{f})$, which is higher for solutions which fulfil the a priori condition. Instead of maximizing the likelihood $P(\vec{y}|K,\vec{f})$ we can then rather maximize the a posteriori likelihood:

$$P\left(\vec{f}\middle|K,\vec{y}\right) = \frac{P\left(\vec{y}\middle|K,\vec{f}\right)P\left(\vec{f}\right)}{P(\vec{y})} \tag{3}$$

Transforming the problem into a minimization of its negative logarithm to facilitate computation, we obtain:

$$\begin{aligned}\operatorname{argmin}_{\vec{f}}\left\{-\log P\left(\vec{f}\middle|K,\vec{y}\right)\right\} &= \operatorname{argmin}_{\vec{f}}\left\{-\log P\left(\vec{y}\middle|K,\vec{f}\right)-\log P\left(\vec{f}\right)+\log P(\vec{y})\right\} = \operatorname{argmin}_{\vec{f}}\Big\{ \\ &-\log P\left(\vec{y}\middle|K,\vec{f}\right)-\log P\left(\vec{f}\right)\Big\}\end{aligned} \tag{4}$$

where also the term $\log P(\vec{y})$ was dropped as it is independent of $\vec{f}$ and as a constant offset does not influence the location of the minimum. Again we refer to Kandlikar and Ramachandran (1999) for a detailed mathematical overview, while in this work, we will focus on some selected approaches and their applicability to combine several instruments in the sub-10 nm range.

2.1. Point-by-point inversion for mobility spectrometers

For completeness, we will start with the description of the simple inversion often used for electrical mobility spectrometers using a DMA for size-classification. In that case, it is assumed that the transfer function of the DMA is rather narrow (Jiang, Attoui, et al., 2011; Jiang, Chen, Kuang, Attoui, & McMurry, 2011). This also holds for most applications in the sub-10 nm range, even if the transfer function is significantly broadened by diffusion (M. R. Stolzenburg, 1988; M. R. Stolzenburg & McMurry, 2008). Altogether, the kernel function of a mobility spectrometer is described by:

$$K_i(d_p) = f_c(d_p)\cdot\eta_{CPC}(d_p)\cdot\eta_{samp}(d_p)\cdot\Omega_{DMA}\left(d_p^i,d_p\right) \tag{5}$$

where $f_c(d_p)$ is the charged fraction of aerosol particles, $\eta_{CPC}(d_p)$ is the counting efficiency of the used condensation particle counter (including detector flow rate and integration time of the measurement), $\eta_{samp}(d_p)$ is the penetration efficiency of the sampling lines of the instrument and $\Omega_{DMA}(d_p^i,d_p)$ is the transfer function of the DMA of the i-th channel with a centroid diameter d_p^i, inferred from the applied voltage and geometry of the DMA (M. R. Stolzenburg & McMurry, 2008) or calibrations with mobility standards (Ude & de la Mora, 2005). In the sub-10 nm regime, where multiple charging of aerosol particles is negligible, the transfer function of a single channel i consists of one approximately lognormal shaped peak (Stolzenburg & McMurry, 2008). If we assume that, neither $f_c(d_p^i)$ nor $\eta_{CPC}(d_p)$, $\eta_{samp}(d_p)$ and $f(d_p)$ change significantly over the width of this peak, the integral of Eq. (1) is reduced to:

$$y_i = f_c\left(d_p^i\right)\cdot\eta_{CPC}\left(d_p^i\right)\cdot\eta_{samp}\left(d_p^i\right)\cdot f\left(d_p^i\right)\int\Omega_{DMA}\left(d_p^i,d_p\right)\,\mathrm{d}d_p = f_c\left(d_p^i\right)\cdot\eta_{CPC}\left(d_p^i\right)\cdot\eta_{samp}\left(d_p^i\right)\cdot f\left(d_p^i\right)\cdot\beta \tag{6}$$

where β is the integrated transfer-function which corresponds to the ratio of aerosol to sheath flow for a balanced standard DMA. Eq. Eqn 6 can be easily solved separately for the size distribution value f at d_p^i for all available n channels of the mobility spectrometer. This justifies the name point-by-point inversion used in the following. For the case of larger particles, multiple charging becomes more important and the kernel functions are not described by single sharp peaks in the size-space. In that case, a specific selection of the analysed voltages set at the DMA can still provide an analytical solution to the problem (Reischl, 1991). However, most algorithms which are widely applied in the community use some linear least-square regression (searching for $\min_{\vec{f}\geq 0}\|\vec{y}-K\vec{f}\|^2$) to solve the problem (Wiedensohler et al., 2012). However, this is known to produce some unwanted oscillations in the reconstructed size-distributions (Sipkens, Olfert, & Rogak, 2020a) and it is very sensitive to noise, especially outliers which are not well described by the underlying Gaussian error assumption.

2.2. Non-linear iterative regression

Twomey (1975) proposed a non-linear iterative algorithm to find a solution to the aerosol size distribution inversion problem. A

good initial guess of the solution $\vec{f}^{0}$, is refined repeatedly by the multiplication (not additive, therefore called non-linear) of correction factors:

$$\vec{f}^{p+1} = [1 + a_1^p K_1] \cdot [1 + a_2^p K_2] \cdot \cdots \cdot [1 + a_n^p K_n] \cdot \vec{f}^{p} \tag{7}$$

where the correction terms a_i^n are simply the ratio of the actual instrument response to the calculate response of the trial solution:

$$a_i^n = \left(\frac{y_i}{\sum_j K_{i,j} f_j} - 1 \right) \tag{8}$$

The algorithm requires the problem to be scaled with $|K_{i,j}| \leq 1$, which makes it challenging to include an error term into the procedure which could account for different uncertainties in the different channels (Sipkens et al., 2020a). If the higher order terms are neglected, we see that this routine corresponds to an expansion of the solution into the Kernel functions:

$$\vec{f}^{p+1} = [1 + a_1^p K_1 + a_2^p K_2 + \cdots + a_n^p K_n] \cdot \vec{f}^{p}. \tag{9}$$

However, also this procedure can lead to artificial oscillations in the solution. Markowski (1987) improved Twomey's algorithm by introducing a smoothing loop after each iteration of Eq. (7). Smoothing was performed by applying a weighted average to neighbouring points of the solution:

$$f\left(d_p^j\right) = \frac{f\left(d_p^{j-1}\right)}{4} + \frac{f\left(d_p^{j}\right)}{2} + \frac{f\left(d_p^{j+1}\right)}{4} \quad j = 2, \ldots, m-1 \tag{10}$$

And for the end points $j = 1, m$ weigting factors of $3/4$ and $1/4$ are chosen for $j = 1, 2$ or $m, m-1$. This procedure continues until a compromise between the agreement of the solution with the data and an arbitrary constraint on the smoothness of the solution is found. Similar versions of this Twomey-Markwoski algorithm have been applied to CPC-battery (Williamson et al., 2018) or impactor measurements (Saari, Arffman, Harra, Rönkkö, & Keskinen, 2018) recently.

2.3. Nullspace optimization

A different approach is presented by Fiebig et al. (2005). It splits the possible solution of $\vec{y} = K\vec{f}$ into two parts $\vec{f} = \vec{f_r} + \vec{f_s}$, where $\vec{f_r}$ assures the fidelity of the solution with the measurement data and $\vec{f_s}$ is an element of the null-space of the kernel matrix K, which does not change the instrument response of $\vec{f}$, i.e. $K\vec{f_s} = \vec{0}$. First, the fidelity term is found by singular value decomposition (SVD) of the kernel matrix K. SVD factorizes the kernel matrix into three component matrices $K = U\Sigma V^T$, where Σ is a diagonal matrix with the singular values σ_j of the kernel matrix K as the non-zero entries. U and V are orthonormal matrices and the column vectors of U corresponding to the non-zero values of Σ form a base of rank k and the column vectors of V corresponding to the zero values of Σ form a base of the nullspace of k. The pseudo-inverse of k is easily calculated from the SVD:

$$\vec{f_r} = V \operatorname{diag}\left(\frac{1}{\sigma_j}\right) U^T \vec{y} \tag{11}$$

The nullspace base V_0 obtained from V is used to find $\vec{f_s}$ with $\vec{f_s} = V_0 \vec{a}$ satisfying a smoothness criteria of the solution. This smoothness criteria is formulated with the finite-difference representation of the second derivative in matrix notation J (see Donatelli and Reichel (2014) for the used antireflective boundary conditions). Compared to the weighted average of the non-linear iterative regression, this leads to a more global measure of smoothness to be minimized via:

$$\min_{\vec{a}} \| J\left(\vec{f_r} + V_0 \vec{a}\right) \|^2, \text{ with } \vec{f_r} + V_0 \vec{a} > \vec{0} \tag{12}$$

In brief, this algorithm searches for a vector of the nullspace of K, which can be added to the pseudo-inverse under the condition that the final solution is as smooth as possible. However, in the case of increasing available instrument information (increasing number of size channels, broad coverage of all sizes by the available kernel functions and large differences in the order of magnitude of different kernel functions K_i), the nullspace might be vanishing and convergence of the algorithm is too slow. Therefore, we provide a new version of the algorithm which achieves better results. We used a preconditioning of the problem to achieve a similar order of magnitude for each line equation of Eq. (2), with $\vec{y}'_i = \vec{y}_i / \sum_{j=0}^{m} K_{i,j}$ and $K'_{i,j} = K_{i,j} / \sum_{j=0}^{m} K_{i,j}$. Moreover, to avoid a nullspace with only very small numerical values and thus very slow convergence, we compute $\vec{f_r}$ only from the n_{sgl} largest singular values σ_j (typically $n_{sgl} \sim 5 \ldots 20$) and all column vectors of V corresponding to the smaller singular values are also used as base vectors for the optimization space. This improved convergence speed and smoothness of the results compared to the initial approach from Fiebig et al. (2005). However, the optimal number of used singular values is a priori not known (but is constraint to be smaller than the rank of the matrix K) and needs to be guessed.

2.4. Tikhonov regularization using a Gaussian likelihood

A more general way to solve ill-posed, underdetermined problems is the method of regularization, which replaces the ill-posed problem with a closely related well-posed problem. In a Bayesian sense, i.e. Eq. (3), this can be formulated in terms of incorporating additional a priori knowledge $P(\vec{f})$. We know that typical aerosol size distributions are rather smooth in size, which we can describe by the total second derivative:

$$P\left(\vec{f}\right) \propto e^{-\lambda\left(\sum_{j=0}^{m} \frac{\partial^2 \vec{f}}{\partial d_p^2}(d_j)\right)^2}. \tag{13}$$

Note, that this formulation of the a priori term assumes a Gaussian distributed probability for the second derivative. If we now also assume a Gaussian distributed error with expected value $K_i \vec{f}$ and variance σ_i^2 for the likelihood of a measurement of y_i given K and $\vec{f}$, this can be expressed by:

$$P\left(y_i \middle| K_i, \vec{f}\right) = \frac{1}{\sigma_i \sqrt{2\pi}} e^{-\frac{1}{2}\left(\frac{y_i - K_i \vec{f}}{\sigma_i}\right)^2} \tag{14}$$

This simplifies the minimization problem, i.e. Eq. (4), to:

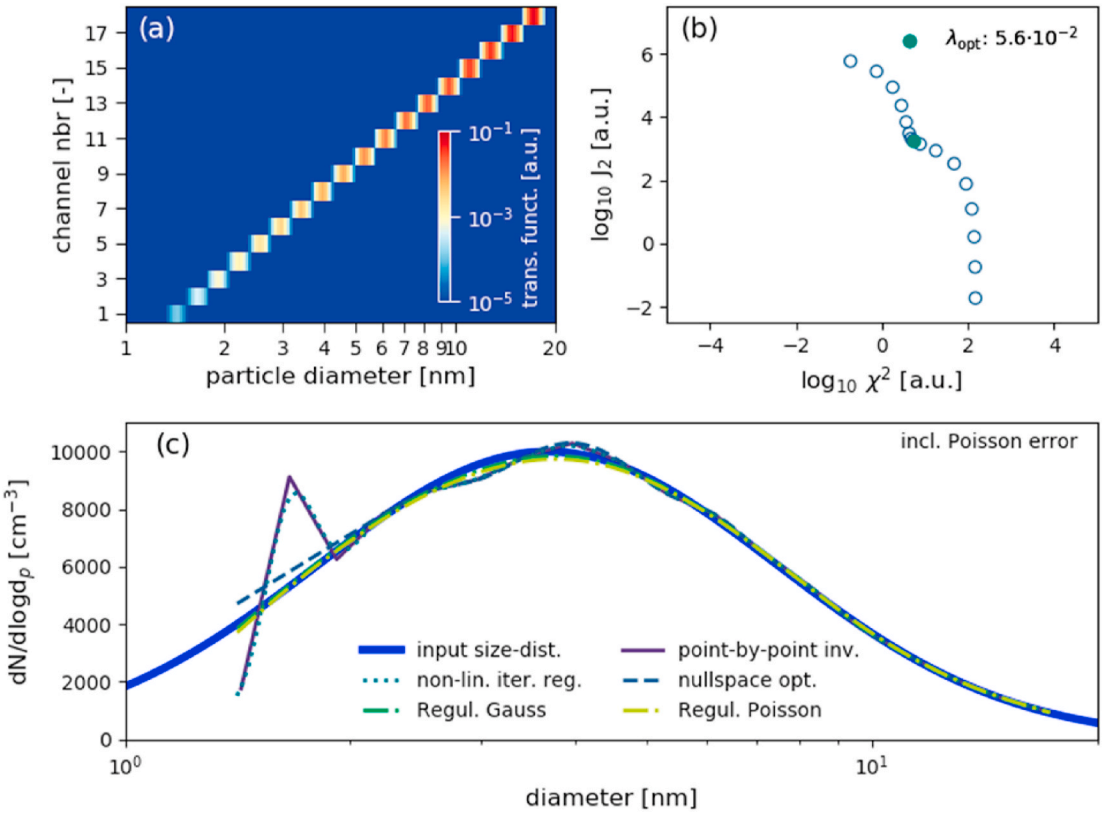

Fig. 1. (a) Shows the kernel function of a HM-DMPS system with the discretized diameters on the ordinate, the channel number on the abscissa and the instrument transfer function represented by the color code. (b) Shows a typical L-curve for optimal regularization parameter estimation with the Tikhonov regularization using Gaussian likelihood, which is also applied to the Poisson based approach. (c) Simple reconstruction of a characteristic size-distribution in the sub-10 nm range. Blue solid line is the input distribution. The dark purple line represents the point-by-point inversion, the turquoise dotted line the non-linear iterative regression, the blue dashed line the nullspace optimization and the green and yellow dashed dotted lines the regularization using Gaussian and Poisson likelihood using the same optimal regularization estimate, respectively. (For interpretation of the references to color in this figure legend, the reader is referred to the Web version of this article.)

$$\begin{aligned}\underset{\vec{f}>0}{\operatorname{argmin}}\left\{-\log P\left(\vec{y}\middle|K,\vec{f}\right)-\log P\left(\vec{f}\right)\right\} &= \underset{\vec{f}>0}{\operatorname{argmin}}\left\{-\sum_{i=0}^{n}\log P\left(y_i|K_i,\vec{f}\right)-\log P\left(\vec{f}\right)\right\}\\ &= \underset{\vec{f}>0}{\operatorname{argmin}}\left\{\sum_{i=0}^{n}\frac{1}{2}\left(\frac{y_i-K_i\vec{f}}{\sigma_i}\right)^2+\lambda\left(\sum_{j=0}^{m}\frac{\partial^2\vec{f}}{\partial d_p^2}(d_j)\right)^2\right\}\\ &= \underset{\vec{f}>0}{\operatorname{argmin}}\left\{\left\|E\left(\vec{y}-K\vec{f}\right)\right\|^2+\left\|\lambda\cdot J\vec{f}\right\|^2\right\}\end{aligned} \tag{15}$$

where the constant offset $\log\frac{1}{\sigma_i\sqrt{2\pi}}$ can be dropped as it is independent of $\vec{f}$. Eq. (15) is identical to the formulation of so-called Tikhonov regularization (Tikhonov & Arsenin, 1977) which adds a second term in the minimization of the least-square regression. This so-called regularization term includes a smoothness requirement on the solution similar to the nullspace optimization. In fact, Hansen (2000) demonstrates that both regularization and nullspace optimization are indeed based on the same principle of the singular value decomposition of the kernel matrix. Compared to Tikhonov and Arsenin (1977), where the identity matrix is used in the regularization term, we again apply the finite-difference representation of the second derivative with antireflective boundary conditions. Transformations to the Tikhonov form is possible using the generalized singular value decomposition (GSVD; e.g. Hansen, 1998) of the matrix pair (EK,J). We refer to the recent work from Petters (2021) for a detailed programming package including such possible transformations of the problem and only apply the regularization scheme of Eq. (15) for our purposes. After the problem is regularized, the optimal regularization parameter λ has to be found, as it is a priori not known. However, different to nullspace optimization, several analytical methods for a good choice of λ exist. The L-curve method (e.g. Hansen, 1992) tries to find a balance between the fidelity term of the solution $\chi^2=\|E\left(\vec{y}-K\vec{f}\right)\|^2$ including the error matrix E (see e.g. Wolfenbarger & Seinfeld, 1990) and the smoothness term of the solution $J_2=\|J\vec{f}\|^2$. The L-curve is a plot where $\log_{10}J_2$ is plotted versus $\log_{10}\chi^2$ for a range of different values of λ often having a clear L-shape appearance (see Fig. 1b for an example). The smallest values of λ yield solutions located in the upper left of the L-curve, while the smoothest solutions with large values of λ are found to the lower right of the L-curve. The optimal solution is located at the corner of the L-curve where a good trade-off between fidelity and smoothness is found. Finding the corner point of such an L-curve shaped curve is a geometrical problem that can be solved numerically and different algorithms for the L-curve corner detection exist (Castellanos, Gómez, & Guerra, 2002; Cultrera & Callegaro, 2020; Hansen, Jensen, & Rodriguez, 2007; Viloche Bazán & Francisco, 2009). We use the simple triangular method proposed by Castellanos et al. (2002), however this might yield overly smooth results or cause problems when several corner-like points exist (Hansen, 2000). Again, we refer to the package by Petters (2021) for a more robust implementation of regularization in the Julia programming language also including other optimal regularization parameter estimates such as generalized cross-validation (Golub, Heath, & Wahba, 1979). Tikhonov regularization has attained already some attention in the inversion of aerosol size-distribution data (Crump & Seinfeld, 1981; Lloyd et al., 1997; Talukdar & Swihart, 2003; Wolfenbarger & Seinfeld, 1990), but application to the combination of several instruments is still lacking.

2.4.1. *Tikhonov regularization using a Poisson likelihood*

The underlying assumption in any least-squared minimization and hence also in the fidelity term of the regularized problem, is that the error $\vec{\varepsilon}$ is normal distributed. However, counting statistics follow inherently a Poisson distribution, which can only be approximated by a Gaussian distribution at large count number. This assumption might not hold in the case of mobility spectrometers measuring in the sub-10 nm range, where particle counts are often below 10 within one measurement cycle.

In order to develop a Poisson formulation of regularization, we express the likelihood $P(\vec{y}\middle|K,\vec{f})$ by a Poisson term:

$$P\left(\vec{y}\middle|K,\vec{f}\right)=\frac{\left(K_i\vec{f}\right)^{y_i}e^{-K_i\vec{f}}}{y_i!} \tag{16}$$

which has $\mathbb{E}(y_i)=\mathrm{Var}(y_i)=K_i\vec{f}$. Inserting Eq. (16) into Eq. (4), we obtain:

$$\begin{aligned}\operatorname{argmin}_{\vec{f}}\left\{-\log P\left(\vec{f}\middle|K,\vec{y}\right)\right\} &= \operatorname{argmin}_{\vec{f}}\left\{\sum_{i}^{n}\left(K_i\vec{f}-y_i\log K_i\vec{f}\right)-\log P\left(\vec{f}\right)\right\}\\ &= \operatorname{argmin}_{\vec{f}}\left\{\sum_{i=0}^{n}\left(K_i\vec{f}-y_i\log K_i\vec{f}\right)+\left\|\lambda\cdot J\vec{f}\right\|^2\right\}\end{aligned} \tag{17}$$

The Poisson distributed counting uncertainty is now inherently incorporated in the first term of Eq. (17). Note that the a priori term still uses a Gaussian assumption similar to classical Tikhonov regularization, therefore we call this approach Tikhonov regularization using a Poisson likelihood. We then use the algorithm proposed by Chambolle and Pock (2011) in order to solve the convex problem of Eq. (17). However, the algorithm is slower than algorithms for the regularized problem using a Gaussian likelihood (Eq. (15)), which can be transformed to a non-negative least square problem (Sipkens et al., 2020a), where fast conventional solvers are available.

Solving the L-curve problem for each inversion would thus not be feasible as many solutions to Eq. (17) need to be computed. We therefore test two different approaches, a single exemplary L-curve regression subsequently applied to all inversions of the same dataset, and the usage of the optimal regularization parameter found by the regularization using a Gaussian likelihood for each individual inversion. Apart from the increasing computational requirement for the optimal regularization parameter estimate, the slower algorithm also induces problems when uncertainty propagation is considered. For the nullspace optimization, Fiebig et al. (2005) suggests a Monte-Carlo approach, which could also be a suitable tool for error propagation in the regularization using a Gaussian likelihood. However, this is also computationally too intensive for our Poisson based approach, requiring faster but more sophisticated methods (e.g. Lucor, Su, & Karniadakis, 2004).

2.5. Kalman smoothing with BAYROSOL

As the above presented methods invert the data for each time step independently, information on the evolution of the aerosol size distribution over time is not incorporated. However, in typical ambient situations changes of the aerosol size distribution are rather slow compared to the acquisition cycle time. One popular approach for solving a time evolution of a system state is the fixed interval Kalman smoother (FIKS; e.g. Kaipio & Somersalo, 2005). In the FIKS framework, not only the observation model for each time step k, i.e. $\vec{y}^k = K\vec{f}^k + \vec{v}^k$ (similar to Eq. (2)), but also evolution model $\vec{f}^{k+1} = F(\vec{f}^k) + \vec{w}^k$ are treated as multivariate random processes. In that sense, the errors $\vec{v}$ and $\vec{w}$ are approximated as Gaussian distributed variables $\mathcal{N}(0,\Gamma_w^k)$ and $\mathcal{N}(0,\Gamma_v^k)$ with the covariance matrices Γ_w^k, Γ_v^k. Our approach is based on the FIKS BAYROSOL (Ozon, Seppänen, et al., 2021), but the problem is simplified by reducing the evolution model of the size-distribution to a random walk model by refraining from estimating the process parameters (nucleation, growth and loss rates of the aerosol system), which are effectively set to zero in the original code, i.e. $\vec{f}^{k+1} = \vec{f}^k + \vec{w}^k$.

The missing non-negativity constraint on the size-distribution is now implemented using a change of variables using the softplus function (Dugas, Bengio, Bélisle, Nadeau, & Garcia, 2001). That way, the Kalman smoother is also applicable to ambient data, where the general dynamics equation (GDE) as underlying evolution model might not always been satisfied without the inclusion of additional source and sink terms accounting for air mass changes. For well-controlled chamber experiments, the GDE approach might achieve more solid results and also provides additional information on the process rates (Ozon, Stolzenburg, Dada, Seppänen, & Lehtinen, 2021). However, as the random walk model is quite far from a realistic evolution model, its uncertainty $\vec{w}^k$ is formally computed as the difference between the GDE model with the unknown process parameters and the zero values used to create the random walk model. As the strongest variations to the size-distribution are expected from growth, we approximate the error via:

$$w_i^k = \Delta t \cdot \left(g_{i-1}^k f_{i-1}^k - g_i^k f_i^k\right) + \mathcal{O}\left(\Delta t^2\right) \tag{18}$$

where Δt is the discretization time step, f_i^k the size-distribution estimated by the FIKS and g_i^k is the unknown growth rate at each time step k and size i which is treated as an independent random variable with the variance $\sigma_{i,w}^2 = 2(\Delta t\, f_i^k\, \sigma_{i,g})^2$ with $\sigma_{i,g}$ fixed to a constant value approximating the maximum uncertainty of the true growth rate. Further different to the original version, we incorporate the correlation in size not only within the covariance of the evolution model by setting $\Gamma_w^k(i,j) = \sigma_{i,w}\sigma_{j,w} \exp\left(-\left(\frac{i-j}{\delta_w}\right)^{a_w}\right)$, but also by using an adjusted measurement operator $H = [K\ \alpha J]$ which includes a regularization term with the above described finite difference approximation of the second derivative J and with adjusted measurement values $\vec{y}' = [\vec{y}\ \vec{0}]$for the measurement update of the FIKS:

$$\vec{y}'^k = H\vec{f}^k + \vec{v}'^k \tag{19}$$

This is similar to the approach by Voutilainen and Kaipio (2001) and improves the results of the FIKS considerably compared to the unregularized measurement update. The difficulty is to find good estimates for the covariance of the error term in the observation model, i.e. $\vec{v}'^k$, and for the regularization parameter α, which is similar to the problem faced in regularization or nullspace optimization. While formulations of Kalman Filters with underlying Poisson statistics exist, e.g. Ebeigbe, Berry, Schiff, and Sauer (2020), our implementation of the FIKS approximates both the uncertainty in the measurement update and the evolution as Gaussian distributed variables, different to the regularization approach using a Poisson likelihood. However, the FIKS incorporates more prior knowledge on the measurement uncertainties compared to the other methods as it includes also error terms for the measurement model similar to Ozon, Stolzenburg, Dada, Seppänen, & Lehtinen, 2021.

3. Results

The above described algorithms were implemented within the python package aeroinverter, which is openly available on GitLab (https://version.helsinki.fi/atm-public/aeroinverter). The Kalman smoother relies on BAYROSOL, which is based on the programming language Julia, but is also available from the same repository. Our implementations of the algorithms might differ from the referred literature as the original code was not openly available. Here, we will present the application of these algorithms to three simulated test cases and two ambient measurements. First, we validate their accuracy with a simple sub-10 nm size-distribution used as input for a single instrument inversion. Then we test the performance upon inclusion of additional instruments with a data set resembling a

nucleation chamber experiment. For a test of a highly complex data set spanning several orders of magnitude and including multiple charging effects for electrical mobility analysers we choose a simulated ambient new particle formation event where we model four DMPS systems and three CPCs. Ultimately, we apply the most robust algorithms to ambient data sets from the SMEAR II and III stations in Hyytiälä and Helsinki, Finland. Table 1 summarizes the included instrumentation and conditions for the different case studies.

3.1. Simple case

First, we tested a very simple case with an idealized size-distribution representative for an engine exhaust aerosol (Alanen et al., 2015). Fig. 1 shows the used kernel, the input size-distribution and the inversion results for all methods except the FIKS, which would require a time series of measurements to be applied. The instrument response $\vec{y}$ is modelled by assuming that an idealized halfmini-DMPS (HM-DMPS; Kangasluoma et al., 2018) with the kernels from Fig. 1a is measuring the input size-distribution shown in Fig. 1c by integrating according to Eq. (1). Note, that the simulated response was inferred from numerical integration with much higher precision than the used discretization of the kernels for the inverse problem. The application of a different forward (calculation of the instrument response) and inverse (reconstruction of the size-distribution) model is essential for avoiding unrealistic good inversion results, the so called "inverse crime" (Colton & Kress, 2013). Additionally, the measured data were corrupted with measurement noise following a Poisson distribution to simulate a classical counting error. Fig. 1c demonstrates that the true size-distribution can be reconstructed reasonably for all methods except for the non-linear iterative regression and point-by-point inversion, which yield a more oscillatory solution below 3 nm. This demonstrates that all presented methods are working reliably when the input number concentration and hence count rates in a single instrument (>20 for all channels of the HM-DMPS) are reasonably high. Generally, the nullspace optimization and non-linear iterative regression are closer to the point-by-point inversion result, while the regularization approaches seem to find a better balance towards the overall smoothness of the solution and are less sensitive to small outliers due to the Poisson noise. An example of an L-curve plot is shown in Fig. 1b for that simple test case, illustrating how the L-curve finds a balance between the fidelity and smoothness of the solution.

3.2. Instrument combination for sub-10 nm inversion: simulated chamber experiment

In order to test the robustness of the inversion algorithms with respect to combining several instruments in the sub-10 nm range into one inversion routine, we use simulated data and modelled instrument responses representative for an aerosol chamber experiment. The aerosol size distribution evolution was modelled similar to Ozon, Seppänen, et al. (2021) using a simple discrete aerosol size distribution model with wall losses and nucleation rates simulating experiments performed in the CERN CLOUD chamber (Kirkby et al., 2011; Stolzenburg et al., 2020) and is shown in Fig. 2a. The modelled instrument responses from the simulated size-distributions are subject to a random counting error with Poisson statistics. We model three different types of instruments for the sub-10 nm range: a HM-DMPS, a DEG-based SMPS (e.g. Jiang et al., 2011a) similar to the PSMPS from Grimm Aerosol GmbH and a CPC-battery (CPCb;

Table 1
Overview over the tested data sets and instruments used for the combining instrument inversion in this study. For all CPCs, the number denotes the 50% detection efficiency cutoff. Systematic offsets for the simulated dataset are applied to the inverse model by shifting the entire kernel function by the denoted value, which was derived by a random assignment once for each test data set.

Case	Instruments	Size-Range	Channels	Syst. Offset
Simple unimodal	HM-DMPS	1.4–17 nm	18	None
Sim. chamber nucleation	HM-DMPS	1.4–9.6 nm	14	+ 9.0%
	PSMPS Grimm Aerosol GmbH	1.4–9.8 nm	55	− 4.7%
	CPC Airmodus A20	>6.7 nm	1	+ 9.8%
	CPC TSI 3772	>9.0 nm	1	− 3.8%
	CPC TSI 3776	>2.8 nm	1	− 5.6%
Sim. ambient NPF/Hyytiälä	HM-DMPS (neg.)	2–15 nm	14	− 3.1%/unknown
	HM-DMPS (pos.)	2–15 nm	14	+ 1.7%/unknown
	Twin-DMPS (nano)	3–40 nm	15	− 4.5%/unknown
	Twin-DMPS (long)	10–998 nm	32	− 3.7%/unknown
	CPC TSI 3775	>7.5 nm	1	− 5.0%/unknown
	CPC TSI 3776	>2.8 nm	1	+ 5.1%/unknown
	PSM-fixed	>1.8 nm	1	+ 0.9%/unknown
Helsinki	HM-DMPS	2.1–14 nm	15	unknown
	PSMPS	2.1–55 nm	92	
	Twin-DMPS (nano)	3.0–40 nm	15	
	Twin-DMPS (long)	15–820 nm	30	
	PSM-scanning	>1.2,>1.4,>1.75,>2.4 nm	4	
	CPC Airmodus A20	>5 nm	1	
	CPC Airmodus A20	>10 nm	1	
	CPC Airmodus A23	>23 nm	1	
	CPC TSI 3025A	>2.8 nm	1	

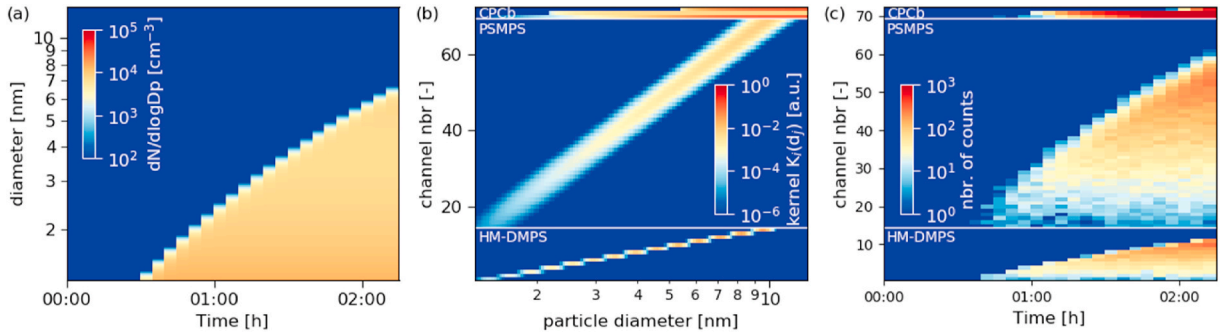

Fig. 2. The chamber nucleation experiment input size distribution used to model the instrument responses is shown in (a). The combined instrument kernel for the inversion of the chamber nucleation data using three different instruments is shown in (b). The discretization diameter is shown on the ordinate, and the different instrument channels are illustrated along the abscissa (different CPCs, stepping voltages and scan discretization for the CPCb, HM-DMPS and PSMPS, respectively). The color code represents the instrument transfer function including the measurement time and analysed aerosol flow rate such that registered counts in the detectors during the measurement interval of the channel can be used as the instrument response vector $\vec{y}$, which is shown in (c) and used as the input for the inversion algorithms. (For interpretation of the references to color in this figure legend, the reader is referred to the Web version of this article.)

Kangasluoma et al., 2014; Kulmala et al., 2007; Williamson et al., 2018). The PSMPS has a lower size resolution and less integration time at each size compared to the HM-DMPS, but provides significantly more size channels between 1.5 and 20 nm. The CPCb consists of three CPCs with different size cutoffs, a TSI Inc. Model 3776 ultrafine CPC (cutoff 2.5 nm), an Airmodus Ltd. A20 CPC (cutoff 6.5 nm), and a TSI Inc. Model 3772 CPC (cutoff 10 nm). Counting efficiencies of the counters were taken from measurements by Wlasits et al. (2020). These three instruments are combined as shown in Fig. 2b and Fig. 2c, which illustrates the differences between the HM-DMPS and PSMPS. The kernels used for simulating the instrument response and the kernels used for the inversion were altered by systematic multiplicative offsets ($K_{\mathrm{inv},i} = e_{\mathrm{syst},i} \cdot K_{\mathrm{forw},i}$). We used normal distributed offsets with mean 1 and 10% standard deviation for each instrument (see Table 1). This simulates imperfect calibrations and other uncertainties often present when estimating the kernel functions. In fact, any inversion combining instruments should be able to find solutions which stabilize these systematic uncertainties in order to provide a reliable result representing the total available information.

Fig. 3 shows the inversion results including all above listed instruments for six different tested inversion routines, the non-linear iterative regression (a), nullspace optimization (b), Tikhonov regularization using Gaussian likelihood (c), and using Poisson

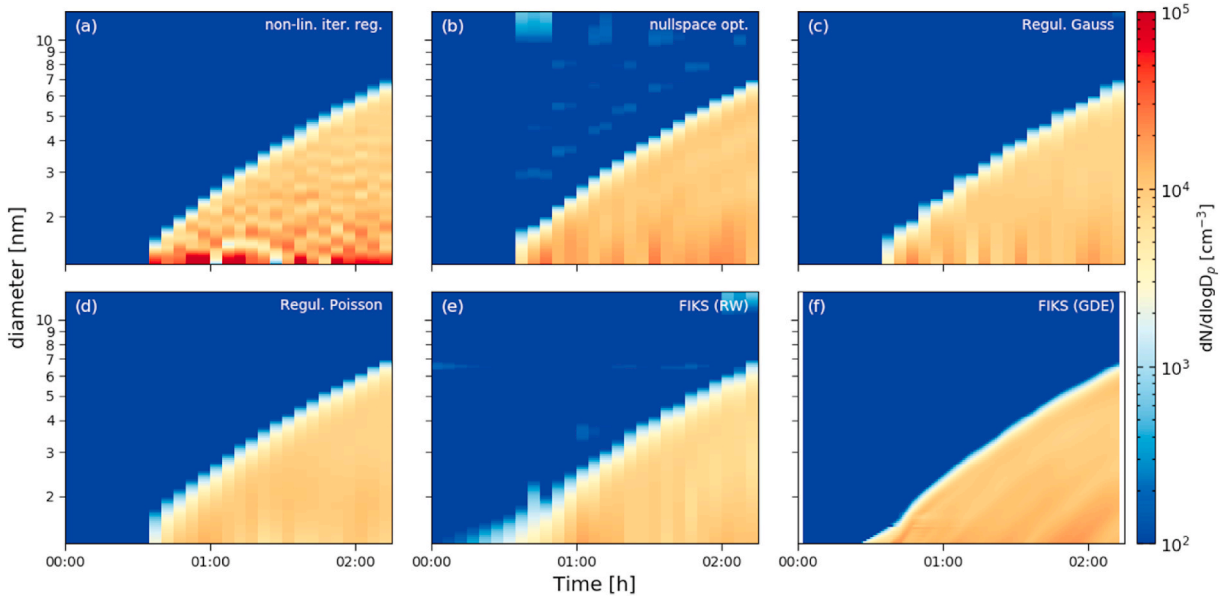

Fig. 3. Inversion results for simulated chamber nucleation experiment (Fig. 2a) combining three different instruments. A HM-DMPS (fewer size channels, higher counting statistics at each channel), a DEG-SMPS (more size channels, lower counting statistics at each channel) and a CPC-battery including three different CPCs measuring the total concentration but with different lower size cutoffs (Fig. 2b). (a) Non-linear iterative regression, (b) nullspace optimization, (c) regularization using a Gaussian likelihood, (d) regularization using a Poisson likihood, (e) FIKS with random walk evolution model, (f) FIKS with general dynamics equation as evolution model.

likelihood (d), and the Kalman smoother with both the random walk (e), and the GDE (f) evolution model. Overall, the agreement of the reconstructed and the input size distribution seems reasonable for most methods considering the underlying noise and the inherent differences and systematic offsets between the instruments. However, there are some remarkable differences in the reconstructed size-distribution.

Apparently, the non-linear iterative regression shows the most oscillatory solutions. This is due to the fact, that the smoothness criteria in this algorithm does not rely on a globally summed measure of smoothness (the operator J), but is achieved by iteratively applying weighted averages. The nullspace optimization and regularization approaches yield better balanced results which provide some degree of smoothness, but still follow fluctuations from the measurement noise. Here, the advantage of the regularization using a Gaussian likelihood is that it does not depend on any unknown a priori assumptions, but finds a good balance between smoothness and fidelity due to the optimal regularization parameter choice via the L-curve method. The regularization using a Poisson likelihood also achieves satisfactory results with less weight to measurement noise at the very small sizes which are mostly affected by Poisson statistics in the two mobility spectrometers (Fig. 2c). Compared to the regularization using a Gaussian likelihood, nullspace optimization and regularization using a Poisson likelihood do not provide an analytical approach for obtaining the optimal number of considered singular values or optimal regularization parameter, respectively. However, also the regularization using the Gaussian likelihood only yields a variation of the optimal regularization parameter within one order of magnitude, which should be even less when the assumed likelihood (i.e. Poisson) is closer to the true likelihood of the measurement. Therefore, we used a single inversion as example case for the Poisson based approach, where we performed the computationally heavy L-curve estimate (see Section 2.4.) and applied the found optimal regularization parameter to all inversions of the dataset. In contrast to this, the number of considered singular values for the nullspace optimization varied significantly between the number of included instruments. But even with a good choice of the unknown parameter, the nullspace optimization reveals difficulties in reconstructing the zero size-distribution at larger sizes, where all measurements yield zero. This might be due to the fact, that true non-negativity is not required within our implementation of the algorithm. However, the slightly relaxed non-negativity constraint, which was necessary to achieve convergence with the chosen solvers, results in oscillations around zero, where there should be a zero reconstruction. Overall, the smoothest solutions are provided by the Kalman smoother due to its inherent additional time correlation in the evolution model. However, the regularization methods and nullspace optimization can better reconstruct the sharp edge of the growing mode and the beginning of the nucleation where the FIKS with the simple random walk evolution model yields an overly smooth result. For the Kalman smoother, we followed the approach of Voutilainen and Kaipio (2001) and tested several choices for $\vec{\nu}^{k}$ and α, finding an acceptable solution for $\alpha = 1$ and $\Gamma_{\nu'}^{k} = \begin{pmatrix} \Gamma_{\nu}^{k} & 0 \\ 0 & 50\mathscr{I} \end{pmatrix}$. Here $\mathscr{I}$ is the identity matrix and Γ_{ν}^{k} is the error of the measurement as defined in Ozon, Seppänen, et al. (2021), Ozon, Stolzenburg, et al. (2021), which contains a term corresponding to a discretization error of the measurement operator and a systematic uncertainty in the measurement operator, which is assumed to be $\Delta H = 0.1H$, i.e. a 10% offset of the device. Ultimately, the most accurate reconstruction of the input size-distribution is achieved by the Kalman smoother using the GDE as evolution model. Note that, it also provides a higher time-resolution in the reconstruction as the time between measurements can be filled by the precise evolution model. This is promising for future applications of this approach including more instruments than shown in Ozon,

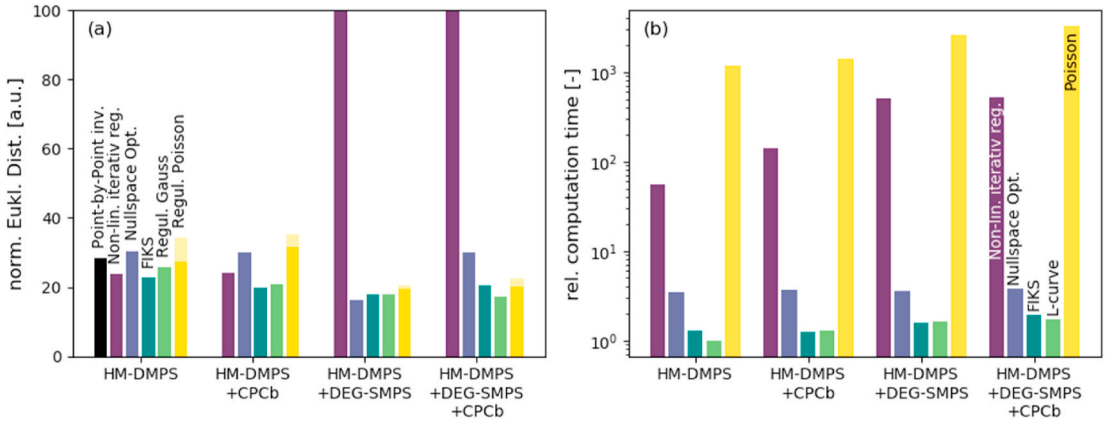

Fig. 4. Effect of instrument combination on the performance of different inversion methods. The normalized (by number of discretization points and inverted measurements) Euclidean Distance of the reconstruction compared to the input size-distribution is shown in (a) versus the different tested instrument combinations. The light bar for the regularization using a Poisson likelihood shows the results obtained when using the same optimal regularization parameter as found for the Gaussian based approach, while the solid yellow bar shows the result from a single exemplary L-curve estimate applied across the dataset. (b) Shows the computation time needed for the different inversions for the entire simulated chamber experiment dataset (2 h 15 min) relative to the fastest algorithm (L-curve for HM-DMPS only case). These values are also close to the absolute computational time in seconds on a standard 4core 1.6 GHz, 16 GB RAM computer, where the regularization using a Gaussian likelihood together with the HM-DMPS data and 128 discretization bins takes roughly 1 s and is subsequently used to normalize all other computational times. (For interpretation of the references to color in this figure legend, the reader is referred to the Web version of this article.)

Stolzenburg, et al. (2021). However, this method is not applicable to data sets from ambient measurements, where too many unknown parameters such as sources and sink terms due to air mass changes might be present.

Besides these reconstructed features of the size-distribution we also tested the performance of the algorithms with respect to speed and the overall fidelity of the reconstruction to the input size distribution. In Fig. 4a we show the normalized Euclidean distance between the reconstructed solution of each algorithm and the input size-distribution for some possible combinations of the three instrument types. Even if upon more available instrument information the systematic uncertainties are increasing, all inversion approaches except for the non-linear iterative regression start to yield decreasing normalized Euclidean distances from the true solution. This demonstrates that such a combined inversion can indeed provide a significant advantage compared to a single instrument approach. This is supported by the fact that all inversion methods achieve a better reconstruction than the point by point inversion in at least some configuration (the non-linear iterative regression only for the single instrument case). The best overall reconstructions with respect to the normalized Euclidean distance to the true solution are achieved by the regularization approaches and FIKS for the multiple instrument cases. For the regularization approaches the one using the Gaussian likelihood achieves slightly better results. The Poisson based method is improved when the optimal regularization parameter is estimated via an exemplary L-curve (the case shown in Fig. 3d) compared to the usage of the Gaussian based regularization parameter retrieval and hence the former approach is used in the following. In terms of algorithm speed, which is shown in Fig. 4b, the regularization using the Gaussian likelihood, nullspace optimization and the FIKS are outperforming the other two algorithms by at least one order of magnitude for the multiple instrument cases. The fast speed of the FIKS could be partly due to its implementation in the faster programming language Julia within BAYROSOL (Bezanson, Edelman, Karpinski, & Shah, 2017). The non-linear iterative regression and the regularization using a Poisson likelihood start to consume significantly more and more time the more instrument information is added. However, considering the fact that the inversion algorithms take less time than the length of the dataset the speed for all algorithms is still acceptable.

3.3. Algorithm test with a highly complex dataset: simulated ambient NPF

Ambient datasets are much more complex than the well-controlled chamber experiments where only one size-distribution mode is constantly growing. We therefore test our algorithms also with a simulated ambient new particle formation event, similar to Ozon, Seppänen, et al. (2021), where more than one aerosol mode is present after the onset of new particle formation. Our modelled instruments are equal to the ones used in the measurements at the SMEAR II station in Hyytiälä, Finland. This includes a HM-DMPS measuring both positively and negatively charged particles. The usage of both could reduce systematic uncertainties due to bipolar diffusion charging (Chen, McMurry, & Jiang, 2018). The CPCb consists of an Airmodus PSM operated a fixed saturator flow rate (cutoff 1.8 nm), a TSI Inc. Model 3776 (cutoff 2.8 nm) and a TSI Inc. Model 3775 (cutoff 7.5 nm). The size range larger than 10 nm is now covered by differential mobility spectrometers with longer classification range and lower resolution. We thus modelled a twin-DMPS similar to Aalto et al. (2001) measuring down to 3 nm, which consist of two DMPS systems one covering the 3–40 nm range and the other the 10–1000 nm range. These devices further need to account for multiple charging of the sampled aerosol, which increases significantly above 10–20 nm (Wiedensohler, 1988) and complicates the inversion (Petters, 2018; Reischl, 1991). The used input size-distribution and combined instrument kernel are shown in Fig. 5. With number concentrations and kernels similar to the chamber nucleation dataset, the mobility spectrometers measuring the smallest sizes are dominated by count rates where the Gaussian approximation of the Poisson error is significant. We show the relative uncertainty which assumed during the inversion and resulting from a pure counting error ($\sigma_{rel} = \sqrt{n}/N$) in Fig. 5c, which is significantly increasing for the sub-10 nm mobility spectrometers and dramatically lower for total particle concentration instruments, i.e. the CPCb.

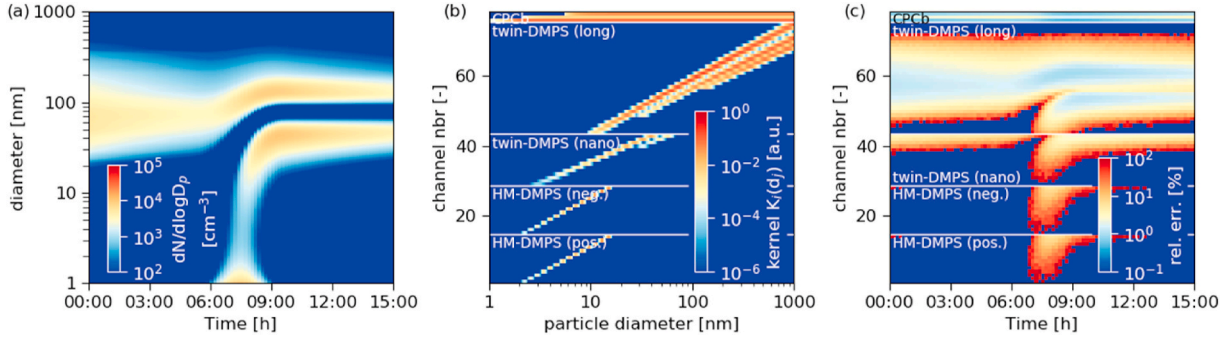

Fig. 5. The simulated ambient new particle formation event input size distribution used to model the instrument responses is shown in (a). The combined instrument kernel for the inversion of the simulated ambient new particle formation data using five different instruments is shown in (b). The discretization diameter is shown on the ordinate, and the different instrument channels are illustrated along the abscissa (different CPCs, stepping voltages and scan discretization for the CPCb, twin-DMPSs and HM-DMPSs, respectively). The color code represents the instrument transfer function including the measurement time and analysed aerosol flow rate such that registered counts in the detectors during the measurement interval of the channel can be used as the instrument response vector $\vec{y}$. The in the inversion procedures assumed relative uncertainty in percent resulting from a pure counting error $\boldsymbol{\sigma} = \sqrt{N}/N$ is shown in (c). (For interpretation of the references to color in this figure legend, the reader is referred to the Web version of this article.)

The reconstructions for the simulated ambient NPF event are presented in Fig. 6. They show that the L-curve regularization, the Poisson algorithm and also the FIKS are able to cope with the above mentioned challenges of a complex data set. For the nullspace optimization it is impossible to find a good number of singular values used in the fidelity estimate to provide reasonable results over the entire size-range of the dataset. Focusing on the sub-10 nm range, the regularization approaches reasonably reconstruct the onset of new particle formation above the lowest instrument detection threshold at 1.8 nm (see Table 1). However, there appears a slight gap in the regularization using a Gaussian likelihood in the sub-3 nm range where the counting statistics of the HM-DMPS are very low (<5 counts) and other information is only available from the fixed-PSM. This is apparently better reconstructed in the regularization using a Poisson likelihood by using the correct uncertainty statistics. The FIKS generally tends to reconstruct lower values in the sub-3 nm range and has difficulties in reproducing the exact onset of new particle formation. However, above 3 nm the results are very close to the input size distribution, indicating that the FIKS with the simple random walk evolution model can be used for complex datasets spanning several orders of magnitudes. This was achieved by a formulation of the covariance of the measurement operator, which requires more smoothness whenever less instrument information is available through the definition of an information indicator $I(d_j) = \sum_i K_i(d_j)$ with $\Gamma_y^k = \begin{bmatrix} \Gamma_v^k & 0 \\ 0 & a(f^{k-1}(d_j)I(d_j)^2)\mathscr{I} \end{bmatrix}$. This accounts for the increased complexity of such a data set, but similar to other approaches the scaling constant a and the regularization parameter α remain a priori unknown. However, we find reasonable results for $\alpha = 1$ and $a = 10000$ by trial-and-error and as this dataset includes the same instrument configuration than deployed in Hyytiälä, we assume that the found parameters for the FIKS can be used on field data too. This is similar to Voutilainen and Kaipio (2001), who found that for similar datasets the optimal estimates of the adjustable parameters in the FIKS remain similar.

In Fig. 7 we show the spread of the reconstructed results compared to the input size-distribution, which confirms the above qualitative observations. The nullspace optimization shows the largest deviations between reconstruction and input, with many off-diagonal reconstructed values for high and low number concentrations. The best correlation is achieved by the regularization using a Gaussian likelihood. The regularization using a Poisson likelihood and the FIKS show slightly more off-diagonal values but still acceptable correlation coefficients, especially at large number concentrations. The off-diagonal entries from the FIKS with significantly larger reconstruction than the input originate from the initialization of the FIKS and thus the first couple of deviating results. Generally, the instrument information below 2 nm is really sparse, which leads to some zero reconstructions for actual non-zero input values for all of the three methods, however, the least for the Poisson case, where low counting statistics are treated more precisely. For the reconstructions above 3 nm we generally find satisfactory results, however when comparing quantities of interest as the particle formation (J_3) and growth rate (GR) as presented in Table 2, we find an overall underestimation of all reconstruction methods compared to the values retrieved from the input size-distribution. The reconstruction via the regularization using a Gaussian likelihood

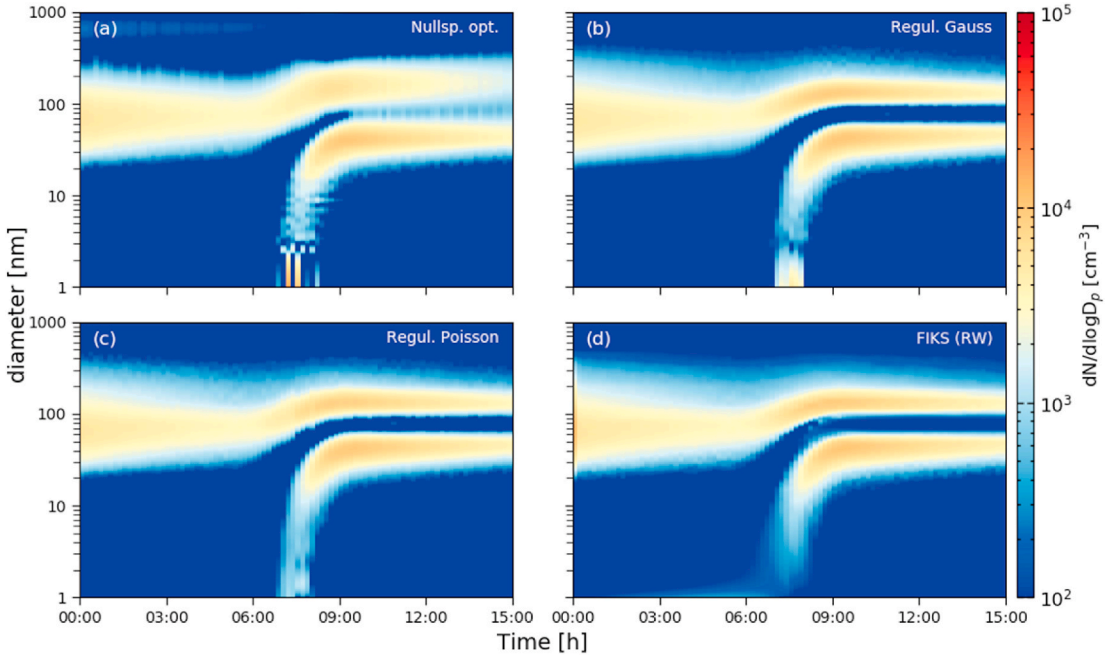

Fig. 6. Inversion results for the more complex simulated dataset representing ambient new particle formation. In total, 4 mobility spectrometers and 3 CPCs were combined for the inversion. (a) Shows the results from the nullpsace optimization with 30 singular values used for the solution space. (b) Shows the standard regularization with the L-curve method for optimal regularization parameter estimation. (c) Shows the Poisson formulation of regularization including a weighting for the systematic uncertainties of the different instruments. (d) Shows the FIKS result including the information indicator for the estimate of the regularization part of the measurement model covariance.

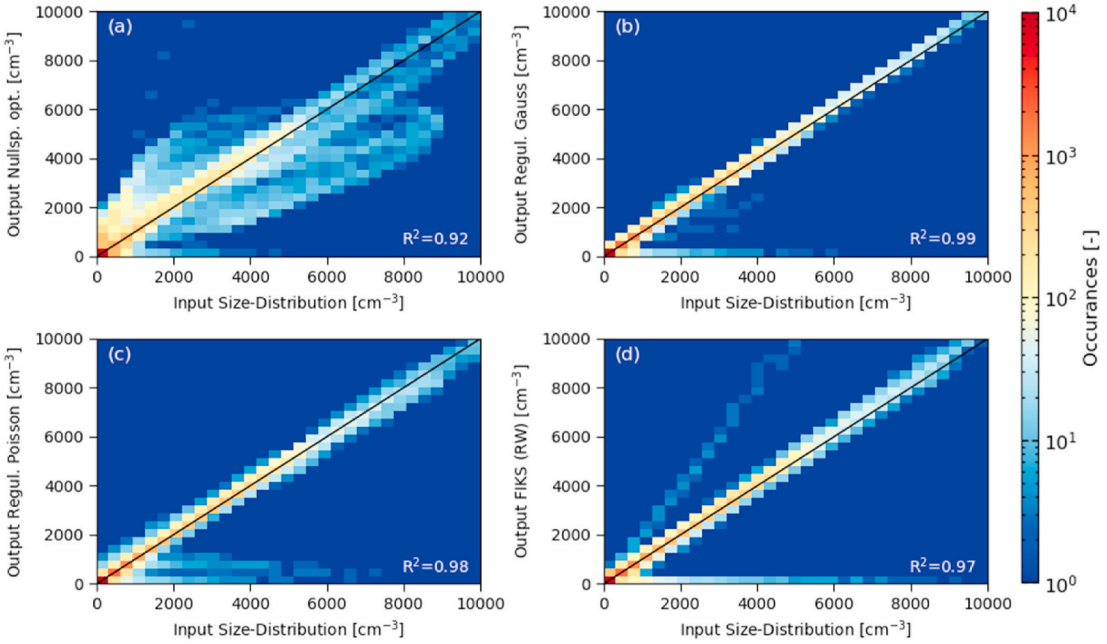

Fig. 7. Binned scatter plot of the reconstructed size-distribution compared to the input size-distribution for the data of Fig. 6. (a) Shows the nullspace optimization, (b) the Tikhonov regularization using a Gaussian likelihood, and using a Poisson likelihood (c) and (d) the FIKS. The Pearson's correlation coefficient for each data set is given in the lower right corner of each panel.

Table 2
Retrieved particle growth rate (GR) and maximum formation rate of 3-nm particles (J_3) using the different reconstructions of the size-distribution as well as the value retrieved from the input-size distribution for the simulated ambient NPF event. Growth rates are calculated using the maximum concentration method and formation rates are evaluated on the interval between 3 and 7 nm, both calculations following the procedure described in Kulmala et al. (2012).

	Input size-dist.	Nullsp. Opt.	Regul. Gauss	Regul. Poisson	FIKS (RW)
GR_{3-7} [nm h-1]	19.0	9.9	16.5	13.0	11.2
J_3 [cm-3 s-1]	0.54	0.32	0.39	0.40	0.29

again finds the best agreement for these parameters within 30% to the values retrieved from the input size-distribution.

3.4. Ambient data inversion

We test our algorithms on two different datasets including multiple particle sizing instruments from two complimentary sites. The first dataset was recorded on the 11th of April 2020 at the SMEAR II station in Hyytiälä, Finland, which is representative for a rural background site in the boreal forest (Hari & Kulmala, 2005). The deployed instrumentation is identical to the one used in the simulated ambient new particle formation case (see Table 1 and Fig. 5b). In order to join the instruments into one inversion routine, the measurement data was averaged into 10 min intervals, typically containing two scans of the HM-DMPS (pos. and neg.) and one scan of the twin-DMPS. We observed much larger fluctuations in the CPCb 1 Hz data during the averaging interval than expected from pure Poisson statistics and thus we modified the assumed error to represent these variations for both the FIKS and regularization using a Gaussian likelihood. Aerosol concentration measurements might be generally influenced by more diverse sources of error than the simple counting error, e.g. fluctuations in flow rates, electronic noise, etc. and more sophisticated error assumptions (e.g. Wilson, Rocke, Durbin, & Kahn, 2004) could be tested in future work. Further, we adjusted the FIKS assumptions and included an error for a possible size-shift in the kernel functions, which is for example expected for the CPCs due to an unknown chemical composition of the sampled particles (Wlasits et al., 2020). However, we found reasonable results for a scaling constant $a = 10000$ and the regularization parameter $\alpha = 1$, i.e. identical than what we identified with the simulated data set in Fig. 4.

In Fig. 8 we compare the inversion results for both regularization approaches, and FIKS (random walk) to the inversion procedure applied to the twin-DMPS data only, which is used to routinely monitor the size-distribution (non-negative least square inversion as in Wiedensohler et al. (2012)). All inversions show that this is a typical new particle formation event day, where a growing nucleation mode appears around noon reaching sizes of up to 20 nm. Compared to the standard approach including only two instruments, the combining instrument algorithms resolve the dynamics of the new particle formation event down to 1–2 nm. In the crucial size range

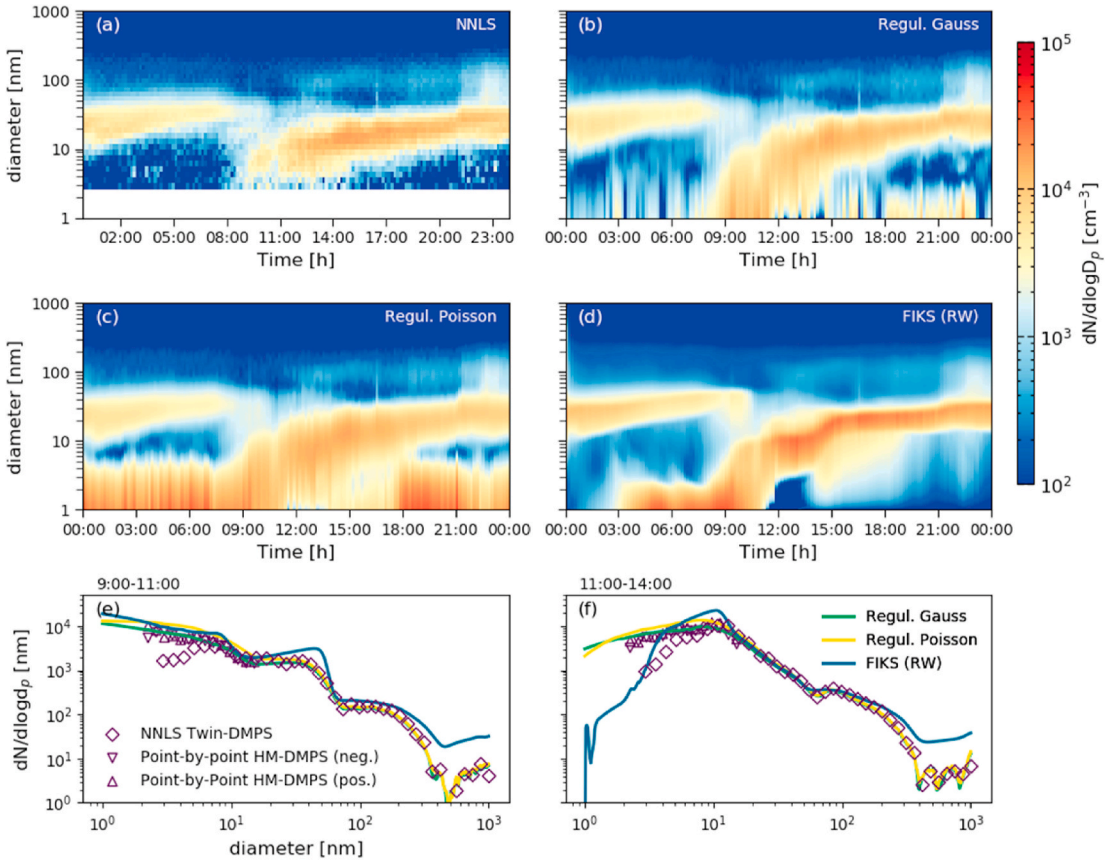

Fig. 8. Inversion results for a data set from the SMEAR II station in Hyytiälä, Finland (April 11th, 2020). (a) Shows the non-negative least-square inversion results which is routinely used for monitoring the size-distribution at SMEAR II. (b) Shows the inversion results using standard regularization with the L-curve for optimal regularization parameter estimation. (c) Shows the results from the regularization using a Poisson likelihood and (d) shows the result from Kalman smoothing using BAYROSOL with the random walk evolution model. (e) and (f) show the median size density over two period of time (9:00–11:00 and 11:00–14:00) for the different methods.

below 10 nm, we can see from the median size-distributions (Fig. 8e and f) that the combining instrument inversions give estimates balancing all available information (also the not individually shown particle counters), whereas the single instrument approaches can have significant offsets from each other. For that reason, the combining approaches can reveal that cluster formation and early growth mainly happens before 11 a.m. (Fig. 8b–d compared to Fig. 8a). After a slight disruption of the air masses and hence the

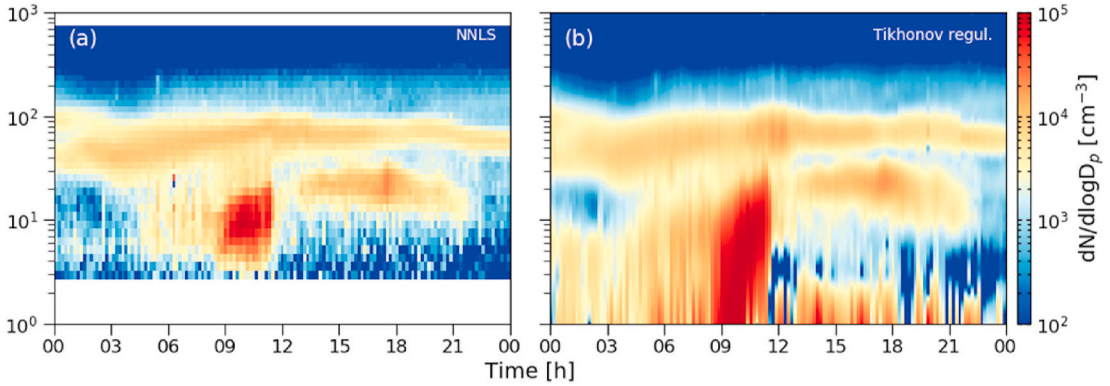

Fig. 9. Inversion results for a data set from the SMEAR III station in Helsinki, Finland (June 12th, 2019). (a) Shows the non-negative least-square inversion results which is routinely used for monitoring the size-distribution at SMEAR III. (b) Shows the inversion results using Tikhonov regularization using a Gaussian likelihood, which was identified to be the most reliable combining instrument inversion procedure for datasets including both mobility spectrometers and total concentration measurements.

size-distribution at around 11 a.m., the afternoon shows a growing nucleation mode without further particle formation. Apart from these common features, there are some distinct differences in the resolved sub-10 nm dynamics. The regularization using a Poisson likelihood indicates a strong presence of sub-3 nm clusters in the morning and evening time and generally slightly higher sub-10 nm concentrations. This is a direct result of the larger error assigned to the particle counters in regularization using a Gaussian likelihood and the FIKS. The Poisson error model might put too much emphasis on the high counted numbers in CPCs, where the actual variations might be higher. Compared to that, the FIKS clearly yields the smoothest results and might be better in removing noise from the data due to its inherent time correlation by the random walk evolution model. However, as can be seen from the median size-distributions, the FIKS result can deviate significantly from the simpler point-by-point and non-negative least-square inversions of the mobility spectrometers, showing some features in the size-distribution which are also not present in the regularization approaches. Moreover, the FIKS is sensitive to a good estimate for the covariance $\Gamma_{\gamma'}^{k}$, which is very challenging and might vary from case to case.

The second dataset was recorded on the 12th of June 2019 at the SMEAR III station in Helsinki, Finland, representative for an urban setting with faster changing conditions (Mølgaard et al., 2016). The sizing instrumentation included in the inversion consists of a twin-DMPS similar to the one used in Hyytiälä, a HM-DMPS measuring negatively charged particles only with an PSM as detector, a PSMPS from Grimm Aerosol GmbH and a CPC battery from Airmodus Ltd., including a PSM in scanning mode (where we used four different saturator flows and their corresponding count rates and calibrations) and three Airmodus Ltd. CPCs tuned to have nominal cutoffs of 5, 10 and 23 nm, together with the routinely operated TSI Inc. CPC Model 3025A. Different to Hyytiälä, no clear new particle formation event with a growing mode is recorded during the day when looking at the standard non-negative least-square reconstruction (Fig. 9a), even if some elevated sub-10 nm concentrations are measured. However, using the most robust combining instrument inversion, classical Tikhonov regularization, we can reveals some dynamics in the sub-10 nm range during the entire day and especially clearly identify a sub-10 nm burst between 9 a.m. and noon (Fig. 9b). Compared to the routinely used non-negative least-square inversion, where no signal is reconstructed at the smallest sizes between 9 and 12 a.m., the regularization using a Gaussian likelihood clearly identifies this as new particle formation, evolving from the very smallest sizes. This demonstrates that combining instruments in the same inversion can actually improve our understanding of NPF and its occurrence.

4. Conclusions

We implemented and tested six different inversion algorithms, which can be used to combine the information of several instruments during the inversion procedure. The popular non-linear iterative regression developed by Twomey (1975) and Markowski (1987) resulted in very oscillatory solutions the more instruments were added to the inversion. The nullspace optimization from Fiebig et al. (2005), was intentionally designed to combine the information of several instruments, but was found to achieve only acceptable results for sub-10 nm aerosol data within a new, modified version, when instrument information overlaps significantly. Moreover, it could not achieve satisfactory results for more complex datasets spanning several orders of magnitude in particle size. Tikhonov regularization is a widely used approach for solving ill-posed inverse problems. It has already been used for solving aerosol size-distribution inversion problems (Crump & Seinfeld, 1981; Lloyd et al., 1997; Wolfenbarger & Seinfeld, 1990). We demonstrated that it is a well-suited approach for inverting chamber and ambient aerosol data from multiple instruments. However, the underlying error assumption is purely Gaussian, which might not hold for the small expected number of counts from mobility spectrometers in the sub-10 nm range. We therefore developed a version of Tikhonov regularization using a Poisson likelihood, which could resolve in full detail a typical new particle formation event in Hyytiälä, which was recorded by four mobility spectrometers and three CPCs simultaneously. Last, we also deployed a recently developed Kalman smoothing algorithm (Ozon, Seppänen, et al., 2021, Ozon, Stolzenburg, et al., 2021), which was adjusted for the inversion of aerosol size-distribution data from ambient measurements. It also achieved remarkably good results for the simulated data sets, while giving very smooth solutions for the real ambient data when compared to the regularization approaches.

Overall, we demonstrated that combining instruments during the inversion can resolve sub-10 nm aerosol dynamics on a level which is not possible with single instruments only. With a dataset from Helsinki, Finland, we could even show that new particle formation events can be identified more clearly if several instruments are combined into one inversion. The regularization approaches and the Kalman smoothing are promising approaches to increase our understanding of aerosol dynamics by using multiple instruments. We recommend the usage of Tikhonov regularization using a Gaussian likelihood (Section 2.4) for datasets including particle counters and mobility spectrometers. The regularization using a Poisson likelihood (Section 2.4.1) might be powerful in the-sub 10 nm range when only mobility spectrometer data are available, where the low count rates are better treated within the Poisson framework. However, other sources of uncertainty in the measurement are neglected in this approach and our test datasets but could be much more important when inverting real data. We found for example that the variations of total concentration measurements during the necessary averaging interval can be much higher than expected from Poisson statistics, leading to an overestimation of their information within a pure Poisson approach. Compared to the regularization methods, Kalman smoothing (Section 2.5) can provide less noisy results, and incorporates more complex measurement model uncertainties but is at the same time more sensitive to these underlying assumptions and could be misleading if used without great care. However, this can also turn into an advantage, as a more sophisticated error treatment could reduce systematic biases from individual (e.g. mis-calibrated) instruments, as it is easy to implement a measurement operator uncertainty.

Further improvement is foreseen: The Poisson algorithm could be speeded up by using a different solver or a faster programming language. The regularization approaches could also be improved using 2-dimensional inversion enabling correlation of the size distribution in time (Buckley, Kimoto, Lee, Fukushima, & Hogan, 2017; Sipkens, Olfert, & Rogak, 2020b), but possibly increasing the computational costs heavily. That way, both the regularization and FIKS provide a mathematically constrained measure of smoothness

in time and size, which should be superior to the proposed post-processing smoothing as suggested by Kulmala et al. (2012). The Kalman smoothing could be updated in order to include the different measurement times of scanning instruments, which then should yield better estimates for fast changing aerosols, as demonstrated in Voutilainen and Kaipio (2001). Last, it would be beneficial if also other instruments could be included in the inversions. For example the neutral cluster and air ion spectrometer (NAIS; Manninen et al., 2009) is frequently used to monitor new particle formation. Due to large uncertainties in the kernel functions of the particle mode we refrained from including it into the inversions, but future work could resolve this. In general, good calibrations and uncertainty estimates of these are essential prerequisites for combining instrument inversions and the systematic error treatment of the Poisson and Gaussian approaches should be further developed in the future.

Ultimately, the demonstrated improvement in inversion of sub-10 nm particle size distributions could then lead to the wide application of more sophisticated analysis tools (e.g. Pichelstorfer et al., 2018). This will resolve the dynamics in the sub-10 nm range on an unprecedented level, increasing our understanding of new aerosol survival during atmospheric new particle formation. An important prerequisite for this would be the wide deployment of comprehensive instrument arrays in the sub-10 nm range in ambient studies, which besides the standard DMPS systems, also includes at least one mobility spectrometer optimized for sub-10 nm detection and supporting CPCs, especially PSMs or others for sub-3 nm detection. Our results clearly show that denser instrument information always benefits the inversion results and hence the deployment of more well-characterized instruments in this crucial size-range is generally recommended.

Data availability

Current version of the code can be found on https://version.helsinki.fi/atm-public/aeroinverter, the version upon submission including the analysis input data is achieved under https://doi.org/10.23729/115c138d-145f-4d96-b53a-47bdbe7a8ecf. Access to raw data will be given by the corresponding author upon reasonable request.

Declaration of competing interest

The authors declare that they have no known competing financial interests or personal relationships that could have appeared to influence the work reported in this paper.

Acknowledgements

We thank Joonas Vanhanen and Airmodus Ltd. as well as Gerhard Steiner and Grimm Aerosol GmbH for providing measuring instruments at the SMEAR II and SMEAR III stations used for the analysis of the ambient datasets. We further thank Lauri Ahonen, Janette Mäkipää and Zoé Brasseur for maintaining the instruments during the field measurements. This research has received funding from the European Union's Horizon 2020 research and innovation programme under the Marie Sklodowska-Curie grant agreement no. 895875 ("NPF-PANDA"). The work is also supported by Academy of Finland via Center of Excellence in Atmospheric Sciences (project no. 272041) and European Research Council via ATM-GTP (742206) and CHAPAs (850614). This research has also received funding from Academy of Finland (project no. 1325656 & 316114, 315203, 307537), Jane and Aatos Erkko Foundation and Academy of Finland Flagship funding (grant no. 337549 and grant no. 337550) and a University of Helsinki three-year grant 75284132.

References

Aalto, P., Hämeri, K., Becker, E., Weber, R., Salm, J., Mäkelä, J. M., et al. (2001). Physical characterization of aerosol particles during nucleation events. *Tellus B: Chemical and Physical Meteorology, 53*(4), 344–358. https://doi.org/10.3402/tellusb.v53i4.17127

Alanen, J., Saukko, E., Lehtoranta, K., Murtonen, T., Timonen, H., Hillamo, R., et al. (2015). The formation and physical properties of the particle emissions from a natural gas engine. *Fuel, 162*, 155–161. https://doi.org/10.1016/j.fuel.2015.09.003

Bauer, P. S., Amenitsch, H., Baumgartner, B., Köberl, G., & Rentenberger, C. (2019). In-situ aerosol nanoparticle characterization by small angle X-ray scattering at ultra-low volume fraction. *Nature Communications, 10*(1), 1122. https://doi.org/10.1038/s41467-019-09066-4

Bezanson, J., Edelman, A., Karpinski, S., & Shah, V. B. (2017). Julia: A fresh approach to numerical computing. *SIAM Review, 59*(1), 65–98. https://doi.org/10.1137/141000671

Buckley, D. T., Kimoto, S., Lee, M.-H., Fukushima, N., & Hogan, C. J. (2017). Technical note: A corrected two dimensional data inversion routine for tandem mobility-mass measurements. *Journal of Aerosol Science, 114*, 157–168. https://doi.org/10.1016/j.jaerosci.2017.09.012

Carslaw, K. S., Lee, L. A., Reddington, C. L., Pringle, K. J., Rap, A., Forster, P. M., et al. (2013). Large contribution of natural aerosols to uncertainty in indirect forcing. *Nature, 503*, 67–71. https://doi.org/10.1038/nature12674

Castellanos, J. L., Gómez, S., & Guerra, V. (2002). The triangle method for finding the corner of the L-curve. *Applied Numerical Mathematics, 43*(4), 359–373. https://doi.org/10.1016/S0168-9274(01)00179-9

Chambolle, A., & Pock, T. (2011). A first-order primal-dual algorithm for convex problems with applications to imaging. *Journal of Mathematical Imaging and Vision, 40*(1), 120–145. https://doi.org/10.1007/s10851-010-0251-1

Chen, X., McMurry, P. H., & Jiang, J. (2018). Stationary characteristics in bipolar diffusion charging of aerosols: Improving the performance of electrical mobility size spectrometers. *Aerosol Science & Technology, 52*(8), 809–813. https://doi.org/10.1080/02786826.2018.1479058

Colton, D., & Kress, R. (2013). *Inverse acoustic and electromagnetic scattering theory* (3rd ed.). Springer-Verlag. https://doi.org/10.1007/978-1-4614-4942-3

Crump, J. G., & Seinfeld, J. H. (1981). A new algorithm for inversion of aerosol size distribution data. *Aerosol Science & Technology, 1*(1), 15–34. https://doi.org/10.1080/02786828208958576

Cultrera, A., & Callegaro, L. (2020). A simple algorithm to find the L-curve corner in the regularisation of ill-posed inverse problems. *IOP SciNotes, 1*(2), 25004. https://doi.org/10.1088/2633-1357/abad0d

Donatelli, M., & Reichel, L. (2014). Square smoothing regularization matrices with accurate boundary conditions. *Journal of Computational and Applied Mathematics, 272*, 334–349. https://doi.org/10.1016/j.cam.2013.08.015

Dugas, C., Bengio, Y., Bélisle, F., Nadeau, C., & Garcia, R. (2001). Incorporating second-order functional knowledge for better option pricing. In T. Leen, T. Dietterich, & V. Tresp (Eds.), *Advances in neural information processing systems* (Vol. 13). MIT Press https://proceedings.neurips.cc/paper/2000/file/44968aece94f667e4095002d140b5896-Paper.pdf.

Ebeigbe, D., Berry, T., Schiff, S. J., & Sauer, T. (2020). Poisson Kalman filter for disease surveillance. *Phys. Rev. Res., 2*(4), 43028. https://doi.org/10.1103/PhysRevResearch.2.043028

Fiebig, M., Stein, C., Schröder, F., Feldpausch, P., & Petzold, A. (2005). Inversion of data containing information on the aerosol particle size distribution using multiple instruments. *Journal of Aerosol Science, 36*(11), 1353–1372. https://doi.org/10.1016/j.jaerosci.2005.01.004

Flagan, R. C. (1998). History of electrical aerosol measurements. *Aerosol Science & Technology, 28*(4), 301–380. https://doi.org/10.1080/02786829808965530

Golub, G. H., Heath, M., & Wahba, G. (1979). Generalized cross-validation as a method for choosing a good ridge parameter. *Technometrics, 21*(2), 215–223. https://doi.org/10.1080/00401706.1979.10489751

Guo, S., Hu, M., Zamora, M. L., Peng, J., Shang, D., Zheng, J., et al. (2014). Elucidating severe urban haze formation in China. *P. Nat. Acad. Sci. USA, 111*(49), 17373. https://doi.org/10.1073/pnas.1419604111. LP – 17378.

Hagen, D. E., & Alofs, D. J. (1983). Linear inversion method to obtain aerosol size distributions from measurements with a differential mobility analyzer. *Aerosol Science & Technology, 2*(4), 465–475. https://doi.org/10.1080/02786828308958650

Hansen, P. C. (1992). Analysis of discrete ill-posed problems by means of the L-curve. *SIAM Review, 34*(4), 561–580. https://doi.org/10.1137/1034115

Hansen, P. C. (1998). Decompositions and other tools. In *Rank-deficient and discrete ill-posed problems* (pp. 19–44). https://doi.org/10.1137/1.9780898719697.ch2. Society for Industrial and Applied Mathematics.

Hansen, P. C. (2000). The L-curve and its use in the numerical treatment of inverse problems. In P. Johnston (Ed.), *Computational inverse problems in electrocardiology, advances in computational bioengineering* (pp. 119–142). WIT Press.

Hansen, P. C., Jensen, T. K., & Rodriguez, G. (2007). An adaptive pruning algorithm for the discrete L-curve criterion. *Journal of Computational and Applied Mathematics, 198*(2), 483–492. https://doi.org/10.1016/j.cam.2005.09.026

Hari, P., & Kulmala, M. (2005). Station for measuring ecosystem–atmosphere relations (SMEAR II). *Boreal Environment Research, 10*, 315–322.

Jiang, J., Attoui, M., Heim, M., Brunelli, N. A., McMurry, P. H., Kasper, G., et al. (2011). Transfer functions and penetrations of five differential mobility analyzers for sub-2 nm particle classification. *Aerosol Science & Technology, 45*(4), 480–492. https://doi.org/10.1080/02786826.2010.546819

Jiang, J., Chen, M., Kuang, C., Attoui, M., & McMurry, P. H. (2011). Electrical mobility spectrometer using a diethylene glycol condensation particle counter for measurement of aerosol size distributions down to 1 nm. *Aerosol Science & Technology, 45*(4), 510–521. https://doi.org/10.1080/02786826.2010.547538

Kaipio, J., & Somersalo, E. (2005). *Statistical and computational inverse problems*. Verlag: Springer. https://doi.org/10.1007/b138659

Kandlikar, M., & Ramachandran, G. (1999). Inverse methods for analysing aerosol spectrometer measurements: A critical review. *Journal of Aerosol Science, 30*(4), 413–437. https://doi.org/10.1016/S0021-8502(98)00066-4

Kangasluoma, J., Ahonen, L. R., Laurila, T. M., Cai, R., Enroth, J., Mazon, S. B., et al. (2018). Laboratory verification of a new high flow differential mobility particle sizer, and field measurements in Hyytiälä. *Journal of Aerosol Science, 124*(March), 1–9. https://doi.org/10.1016/j.jaerosci.2018.06.009

Kangasluoma, J., Cai, R., Jiang, J., Deng, C., Stolzenburg, D., Ahonen, L. R., et al. (2020). Overview of measurements and current instrumentation for 1–10 nm aerosol particle number size distributions. *Journal of Aerosol Science*. https://doi.org/10.1016/j.jaerosci.2020.105584, 105584.

Kangasluoma, J., Junninen, H., Lehtipalo, K., Mikkilä, J., Vanhanen, J., Attoui, M., et al. (2013). Remarks on ion generation for CPC detection efficiency studies in sub-3-nm size range. *Aerosol Science & Technology, 47*(5), 556–563. https://doi.org/10.1080/02786826.2013.773393

Kangasluoma, J., & Kontkanen, J. (2017). On the sources of uncertainty in the sub-3nm particle concentration measurement. *Journal of Aerosol Science, 112* (Supplement C), 34–51. https://doi.org/10.1016/j.jaerosci.2017.07.002

Kangasluoma, J., Kuang, C., Wimmer, D., Rissanen, M. P., Lehtipalo, K., Ehn, M., et al. (2014). Sub-3 nm particle size and composition dependent response of a nano-CPC battery. *Atmos. Meas. Tech., 7*(3), 689–700. https://doi.org/10.5194/amt-7-689-2014

Kirkby, J., Curtius, J., Almeida, J., Dunne, E., Duplissy, J., Ehrhart, S., et al. (2011). Role of sulphuric acid, ammonia and galactic cosmic rays in atmospheric aerosol nucleation. *Nature, 476*, 429–433. https://doi.org/10.1038/nature10343

Kulmala, M., Dada, L., Daellenbach, K. R., Yan, C., Stolzenburg, D., Kontkanen, J., et al. (2021). Is reducing new particle formation a plausible solution to mitigate particulate air pollution in Beijing and other Chinese megacities? *Faraday Discussions*. https://doi.org/10.1039/D0FD00078G

Kulmala, M., Kontkanen, J., Junninen, H., Lehtipalo, K., Manninen, H. E., Nieminen, T., et al. (2013). Direct observations of atmospheric aerosol nucleation. *Science, 339*(6122), 943–946. https://doi.org/10.1126/science.1227385

Kulmala, M., Mordas, G., Petäjä, T., Grönholm, T., Aalto, P. P., Vehkamäki, H., et al. (2007). The condensation particle counter battery (CPCB): A new tool to investigate the activation properties of nanoparticles. *Journal of Aerosol Science, 38*(3), 289–304. https://doi.org/10.1016/j.jaerosci.2006.11.008

Kulmala, M., Petäjä, T., Nieminen, T., Sipilä, M., Manninen, H. E., Lehtipalo, K., et al. (2012). Measurement of the nucleation of atmospheric aerosol particles. *Nature Protocols, 7*(9), 1651–1667. https://doi.org/10.1038/nprot.2012.091

Lloyd, J. J., Taylor, C. J., Lawson, R. S., & Shields, R. A. (1997). The use of the L-curve method in the inversion of diffusion battery data. *Journal of Aerosol Science, 28*(7), 1251–1264. https://doi.org/10.1016/S0021-8502(97)00018-9

Lucor, D., Su, C.-H., & Karniadakis, G. E. (2004). Generalized polynomial chaos and random oscillators. *International Journal for Numerical Methods in Engineering, 60*(3), 571–596. https://doi.org/10.1002/nme.976

Manninen, H. E., Petäjä, T., Asmi, E., Riipinen, I., Nieminen, T., Mikkilä, J., et al. (2009). Long-term field measurements of charged and neutral clusters using Neutral cluster and Air Ion Spectrometer (NAIS). *Boreal Environment Research, 14*, 591–605.

Markowski, G. R. (1987). Improving Twomey's algorithm for inversion of aerosol measurement data. *Aerosol Science & Technology, 7*(2), 127–141. https://doi.org/10.1080/02786828708959153

Mølgaard, B., Vanhatalo, J., Aalto, P. P., Prisle, N. L., & Hämeri, K. (2016). Notably improved inversion of differential mobility particle sizer data obtained under conditions of fluctuating particle number concentrations. *Atmos. Meas. Tech., 9*(2), 741–751. https://doi.org/10.5194/amt-9-741-2016

Ozon, M., Seppänen, A., Kaipio, J. P., & Lehtinen, K. E. J. (2021a). Retrieval of process rate parameters in the general dynamic equation for aerosols using Bayesian state estimation: BAYROSOL1.0. *Geoscientific Model Development, 14*, 3715–3739. https://doi.org/10.5194/gmd-14-3715-2021

Ozon, M., Stolzenburg, D., Dada, L., Seppänen, A., & Lehtinen, K. E. J. (2021b). Aerosol formation and growth rates from chamber experiments using Kalman smoothing. *Atmospheric Chemistry and Physics, 21*, 12595–12611. https://doi.org/10.5194/acp-21-12595-2021

Pedata, P., Stoeger, T., Zimmermann, R., Peters, A., Oberdörster, G., & D'Anna, A. (2015). Are we forgetting the smallest, sub 10 nm combustion generated particles? *Particle and Fibre Toxicology, 12*(1), 34. https://doi.org/10.1186/s12989-015-0107-3

Petters, M. D. (2018). A language to simplify computation of differential mobility analyzer response functions. *Aerosol Science & Technology, 52*(12), 1437–1451. https://doi.org/10.1080/02786826.2018.1530724

Petters, M. D. (2021). A software package to simplify Tikhonov regularization with examples for matrix-based inversion of SMPS and HTDMA data. *Atmos. Meas. Techn. Discuss.*, 1–27. https://doi.org/10.5194/amt-2021-51, 2021.

Pichelstorfer, L., Stolzenburg, D., Ortega, J., Karl, T., Kokkola, H., Laakso, A., et al. (2018). Resolving nanoparticle growth mechanisms from size- and time-dependent growth rate analysis. *Atmospheric Chemistry and Physics, 18*(2), 1307–1323. https://doi.org/10.5194/acp-18-1307-2018

Reischl, G. P. (1991). Measurement of ambient aerosols by the differential mobility analyzer method: Concepts and realization criteria for the size range between 2 and 500 nm. *Aerosol Science & Technology, 14*(1), 5–24. https://doi.org/10.1080/02786829108959467

Saari, S., Arffman, A., Harra, J., Rönkkö, T., & Keskinen, J. (2018). Performance evaluation of the HR-ELPI + inversion. *Aerosol Science & Technology, 52*(9), 1037–1047. https://doi.org/10.1080/02786826.2018.1500679

Sipkens, T. A., Olfert, J. S., & Rogak, S. N. (2020a). Inversion methods to determine two-dimensional aerosol mass-mobility distributions: A critical comparison of established methods. *Journal of Aerosol Science, 140*, 105484. https://doi.org/10.1016/j.jaerosci.2019.105484

Sipkens, T. A., Olfert, J. S., & Rogak, S. N. (2020b). Inversion methods to determine two-dimensional aerosol mass-mobility distributions II: Existing and novel Bayesian methods. *Journal of Aerosol Science, 146*, 105565. https://doi.org/10.1016/j.jaerosci.2020.105565

Stolzenburg, M. R. (1988). *An ultrafine aerosol size distribution system*. University of Minnesota.
Stolzenburg, M. R., & McMurry, P. H. (2008). Equations governing single and tandem DMA configurations and a new lognormal approximation to the transfer function. *Aerosol Science & Technology, 42*, 421–432. https://doi.org/10.1080/02786820802157823
Stolzenburg, D., Simon, M., Ranjithkumar, A., Kürten, A., Lehtipalo, K., Gordon, H., et al. (2020). Enhanced growth rate of atmospheric particles from sulfuric acid. *Atmospheric Chemistry and Physics, 20*(12), 7359–7372. https://doi.org/10.5194/acp-20-7359-2020
Stolzenburg, D., Steiner, G., & Winkler, P. M. (2017). A DMA-train for precision measurement of sub-10 nm aerosol dynamics. *Atmos. Meas. Tech., 10*(4), 1639–1651. https://doi.org/10.5194/amt-10-1639-2017
Swihart, M. T. (2003). Vapor-phase synthesis of nanoparticles. *Curr. Opin. Colloid. In, 8*(1), 127–133. https://doi.org/10.1016/S1359-0294(03)00007-4
Talukdar, S. S., & Swihart, M. T. (2003). An improved data inversion program for obtaining aerosol size distributions from scanning differential mobility analyzer data. *Aerosol Science & Technology, 37*(2), 145–161. https://doi.org/10.1080/02786820300952
Tikhonov, A. N., & Arsenin, V. Y. (1977). *Solutions of ill-posed problems*. Jon Wiley and Sons.
Twomey, S. (1975). Comparison of constrained linear inversion and an iterative nonlinear algorithm applied to the indirect estimation of particle size distributions. *Journal of Computational Physics, 18*(2), 188–200. https://doi.org/10.1016/0021-9991(75)90028-5
Ude, S., & de la Mora, J. (2005). Molecular monodisperse mobility and mass standards from electrosprays of tetra-alkyl ammonium halides. *Journal of Aerosol Science, 36*(10), 1224–1237. https://doi.org/10.1016/j.jaerosci.2005.02.009
Vanhanen, J., Mikkilä, J., Lehtipalo, K., Sipilä, M., Manninen, H. E., Siivola, E., et al. (2011). Particle size magnifier for nano-CN detection. *Aerosol Science & Technology, 45*(4), 533–542. https://doi.org/10.1080/02786826.2010.547889
Vazquez-Pufleau, M., & Winkler, P. M. (2020). Development of an ultraviolet constant angle Mie scattering detector toward the determination of aerosol growth kinetics in the transition and free molecular regime. *Aerosol Science & Technology, 54*(8), 917–928. https://doi.org/10.1080/02786826.2020.1736504
Viloche Bazán, F. S., & Francisco, J. B. (2009). An improved fixed-point algorithm for determining a Tikhonov regularization parameter. *Inverse Problems, 25*(4), 45007. https://doi.org/10.1088/0266-5611/25/4/045007
Viskari, T., Asmi, E., Kolmonen, P., Vuollekoski, H., Petäjä, T., & Järvinen, H. (2012). Estimation of aerosol particle number distributions with Kalman Filtering – Part 1: Theory, general aspects and statistical validity. *Atmospheric Chemistry and Physics, 12*(24), 11767–11779. https://doi.org/10.5194/acp-12-11767-2012
Viskari, T., Asmi, E., Virkkula, A., Kolmonen, P., Petäjä, T., & Järvinen, H. (2012). Estimation of aerosol particle number distribution with Kalman Filtering – Part 2: Simultaneous use of DMPS, APS and nephelometer measurements. *Atmospheric Chemistry and Physics, 12*(24), 11781–11793. https://doi.org/10.5194/acp-12-11781-2012
Voutilainen, A., & Kaipio, J. P. (2001). Estimation of non-stationary aerosol size distributions using the state-space approach. *Journal of Aerosol Science, 32*(5), 631–648. https://doi.org/10.1016/S0021-8502(00)00110-5
Wiedensohler, A. (1988). An approximation of the bipolar charge distribution for particles in the submicron size range. *Journal of Aerosol Science, 19*(3), 387–389. https://doi.org/10.1016/0021-8502(88)90278-9
Wiedensohler, A., Birmili, W., Nowak, A., Sonntag, A., Weinhold, K., Merkel, M., et al. (2012). Mobility particle size spectrometers: Harmonization of technical standards and data structure to facilitate high quality long-term observations of atmospheric particle number size distributions. *Atmos. Meas. Tech., 5*(3), 657–685. https://doi.org/10.5194/amt-5-657-2012
Williamson, C., Kupc, A., Wilson, J., Gesler, D. W., Reeves, J. M., Erdesz, F., et al. (2018). Fast time response measurements of particle size distributions in the 3–60\, nm size range with the nucleation mode aerosol size spectrometer. *Atmos. Meas. Tech., 11*(6), 3491–3509. https://doi.org/10.5194/amt-11-3491-2018
Wilson, M. D., Rocke, D. M., Durbin, B., & Kahn, H. D. (2004). Detection limits and goodness-of-fit measures for the two-component model of chemical analytical error. *Analytica Chimica Acta, 509*(2), 197–208. https://doi.org/10.1016/j.aca.2003.12.047
Wlasits, P. J., Stolzenburg, D., Tauber, C., Brilke, S., Schmitt, S. H., Winkler, P. M., et al. (2020). Counting on chemistry: Laboratory evaluation of seed-material-dependent detection efficiencies of ultrafine condensation particle counters. *Atmos. Meas. Tech., 13*(7), 3787–3798. https://doi.org/10.5194/amt-13-3787-2020
Wolfenbarger, J. K., & Seinfeld, J. H. (1990). Inversion of aerosol size distribution data. *Journal of Aerosol Science, 21*(2), 227–247. https://doi.org/10.1016/0021-8502(90)90007-K